



Title	Low-temperature Synthesis of $\text{MgCr}_2\text{S}_4$ and $\text{Li}_2\text{YCl}_4$ and the Type of Metastability
Author(s)	井藤, 浩明
Citation	北海道大学. 博士(工学) 甲第15411号
Issue Date	2023-03-23
DOI	10.14943/doctoral.k15411
Doc URL	<a href="http://hdl.handle.net/2115/91533">http://hdl.handle.net/2115/91533</a>
Type	theses (doctoral)
File Information	ITO_Hiroaki.pdf



[Instructions for use](#)

Low-temperature synthesis of  $\text{MgCr}_2\text{S}_4$  and  $\text{Li}_3\text{YCl}_6$   
and the type of metastability

Hiroaki Ito

February 2023

1 General introduction	
1-1 high-temperature solid-state reaction	4
1-2 Low-temperature synthesis of materials	4
1-3 Approaches for low-temperature synthesis	4
1-3-1 High-energy ball milling	4
1-3-2 Solid-state metathesis reaction	5
1-3-3 Liquid-assisted solid-state synthesis	5
1-4 Understanding of the synthesis reaction of solid-state materials	6
1-4-1 Thermodynamics of the synthesis reaction of solid-state materials	7
1-4-2 Kinetics of the synthesis reaction of solid-state materials	8
1-5 In-situ X-ray diffraction measurement to understand the synthesis reaction	9
1-6 Selection of materials	9
1-7 Secondary battery materials	9
1-7-1 Ternary spinel sulfide $\text{MgCr}_2\text{S}_4$	10
1-7-2 Ternary chloride $\text{Li}_3\text{MCl}_6$ (M=trivalent element)	11
1-8 Aim and strategies of this work	13
1-9 Contents of this paper	13
1-10 References	15
2 Low-temperature synthesis of $\text{MgCr}_2\text{S}_4$	
2-1 Problems of high-temperature synthesis	20
2-2 Synthesis and properties of $\text{MgCr}_2\text{S}_4$	20
2-3 Aim of this chapter	21
2-4 Metathesis reaction	22
2-5 Experimental	24
2-6 Results	27
2-7 Discussion	35
2-8 Conclusions	39
2-9 References	40
3 Novel polymorphs of $\text{Li}_3\text{YCl}_6$	
3-1 $\text{Li}^+$ -ion conducting ternary halide electrolytes	43
3-2 Aim of this chapter	44
3-3 Experimental section	
3-3-1 Experimental	44
3-3-2 Rietveld Refinement Details	46

3-4 Results	46
3-5 Summary	60
3-5 References	61
 4 The thermodynamic stability of $\text{S-Li}_3\text{YCl}_6$	
4-1 Introduction	
4-1-1 Definition of metastability	63
4-1-2 Variety of observed and hypothetical structures with metastability	64
4-1-3 Examples of metastable materials obtained by different synthesis ways	64
4-1-4 Kinetical representation of synthesis strategies	65
4-1-5 Thermodynamic representation of metastability	66
4-1-6 Evaluation of the energy curve	67
4-1-7 Remnant and intermediate metastability	68
4-1-8 Aim of this chapter	69
4-2 Experimental section	69
4-3 Result: Reversibility of phase transition revealed by XRD measurements	70
4-4 Discussion	71
4-5 Conclusion	73
4-6 References	74
 5 General conclusion	77

## **Chapter1 General Introduction**

### **1-1 high-temperature solid-state reaction**

The simplest and the most fundamental method for synthesizing inorganic materials, such as alloys, glasses, and ceramics, is a solid-state reaction in which the powder starting materials are mixed and heated using a furnace and is also known as the shake-and-bake method<sup>[1-4]</sup>. In the solid-state reaction, the constituent elements of the precursors must diffuse through the contact points between the powders for the reaction to proceed. Due to the slow atomic diffusion in the solid phase, sufficient diffusion of each element is often achieved using high-temperature heating for a long time to obtain a nearly single-phase product. High-temperature heating generally results in the production of a thermodynamically stable product and the agglomeration of product particles.

### **1-2 Low-temperature synthesis of materials**

Lowering the reaction temperature is employed as a fundamental approach to obtaining novel materials. DFT calculation of formation enthalpy indicated that the inorganic materials already synthesized are not always thermodynamically stable<sup>[5]</sup>, and thermodynamically metastable phases can exhibit better performances than stable ones including superconductors<sup>[6, 7]</sup>, catalysts<sup>[8-10]</sup>, and superionic materials<sup>[11-13]</sup>. Furthermore, heating at low temperatures suppresses decomposition at high temperatures, changes in composition due to the volatilization of consistent elements like Sulfur, and aggregation of product particles. The reaction temperature can be altered by using different reaction pathways and starting materials<sup>[1, 14]</sup>, or by using a liquid phase<sup>[15-19]</sup>.

### **1-3 Approaches for low-temperature synthesis**

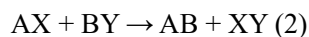
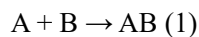
#### **1-3-1 High-energy ball milling**

High-energy ball milling is a mechanical approach to obtaining fine powders, glasses, and amorphous

materials<sup>[20]</sup>. The starting materials are sealed in the pots with balls and rotated at a certain rate. The milling shortens the diffusion length required for the reaction to happen. By using a high-energy planetary ball mill and subsequent heat treatments, sulfide glass and glass ceramics such as  $\text{Li}_3\text{PS}_4$  and  $\text{Li}_7\text{P}_3\text{S}_{11}$  are synthesized and studied as solid electrolytes<sup>[21, 22]</sup>.

### 1-3-2 Solid-state metathesis reaction

Recently, solid-state metathesis reactions have been developed as a thermodynamical approach in which the reaction is initiated by heating at low temperatures and finishes in a short time<sup>[23, 24]</sup>. In the metathesis reaction, the precursors exchange the components with each other and produce materials with byproducts. When the product AB is synthesized by the simple reaction between each element, the reaction can be expressed as the equation (1). The metathesis reaction is generally represented as the following equation (2), where AB is the target material and XY is the byproduct.



The reaction is thermodynamically driven by the large reaction enthalpy enhanced by the formation of thermodynamically stable byproducts. By using an alkali(earth) metal compound and metal halides, many materials such as oxides<sup>[25]</sup>, nitrides<sup>[226, 27]</sup>, and sulfides<sup>[28]</sup> can be obtained with alkali(earth) halides by reaction for several seconds. These reactions generate large amounts of heat and proceed in a self-promoting manner.

### 1-3-3 Liquid-assisted solid-state synthesis

Liquid-assisted solid-state synthesis uses a liquid solvent to accelerate the reaction followed by heating the solution to produce a product powder<sup>[16, 29-31]</sup>. The liquid phase including molten salts, water, and organic solvents provides the uniform distribution of consistent elements which is favorable for the

reaction. The Sol-gel method also has been employed to obtain the oxide materials at low temperatures<sup>[32]</sup>. Oxide solid electrolyte,  $\text{Li}_7\text{La}_3\text{Zr}_2\text{O}_{12}$  (LLZ), usually requires sintering at about 1000 °C or higher to synthesize from oxide precursors<sup>[33]</sup>. The sol-gel method is another way to obtain LLZ only with low-temperature heating around 700 °C<sup>[34]</sup>. More recently, the water vapor-assisted solid-state reaction of dielectric oxide,  $\text{BaZrO}_3$ , is reported<sup>[17]</sup>. In the WASSR, a small amount of water is added to the starting material to accelerate interfacial reactions by covering the particle surface with water and increasing the reaction rate. However, due to the limited theoretical understanding of the reaction, each reaction condition must be determined by experiments.

#### **1-4 Understanding of the synthesis reaction of solid-state materials**

The energy landscape has been used in organic chemistry, physics, and biochemistry. The energy landscape is a multi-dimensional curved surface map that shows the relationship between different configurations and is the function of temperature, pressure, reaction process, precursor structure, and composition. Figure 1-1 shows the schematic image of the energy landscape where four different reactions are represented as colored arrows. By using the energy landscape, it is possible to design the synthesis reaction of the target substance. If the free energy of the target material is the lowest in the reaction pathway and decreases along the reaction proceeds as shown in fig. 1-1 as reaction route 1, the reaction to produce the target material can be successful. When thermodynamically competing materials exist such as route 2, additional treatment is necessary for the selective synthesis. However, creating multi-dimensional energy landscapes for inorganic materials is undergoing since quantitative knowledge is limited. Although the thermodynamic feasibility of a reaction can be predicted from the reaction enthalpy change, the thermodynamic stability does not fully express the synthesizability of target materials<sup>[5]</sup>. Thus, the reactions to synthesize solid-state materials must be understood from both thermodynamics and kinetics.

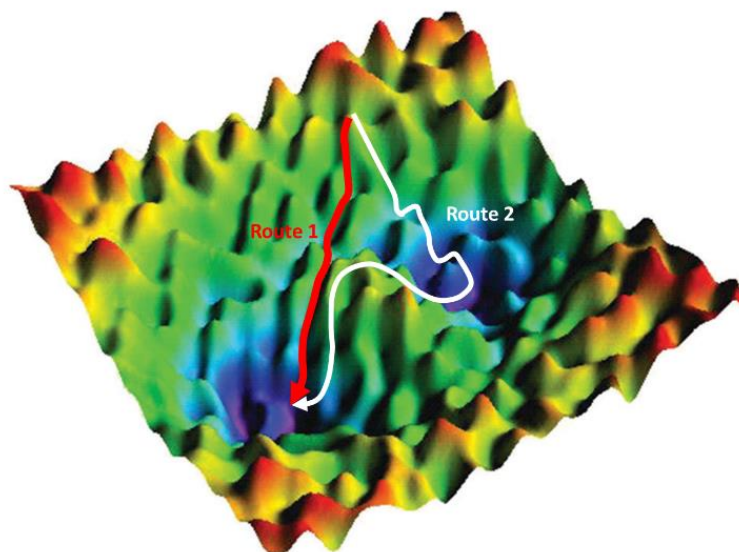


Figure 1-1: Schematic image of energy landscape which visualizes the energy change during the reaction modified from the reported one by M. Dmitri *et al*<sup>[35]</sup>. Red and white arrows were added to represent the possible reaction pathways with different energy minima.

#### 1-4-1 Thermodynamics of the synthesis reaction of solid-state materials

Thermodynamics is the study of the transformations of energy. The free energy change ( $\Delta G$ ) indicates that the reaction can proceed spontaneously when the  $\Delta G$  is negative under ambient conditions.  $\Delta G$  is the sum of the enthalpy change ( $\Delta H$ ) and the product of the absolute temperature ( $T$ ) and the entropy change ( $\Delta S$ ). Phase diagrams and reaction coordinate diagrams are used to explain reactions based on thermodynamics. A phase diagram generally shows the state at a certain point, with composition on the horizontal axis and temperature on the vertical axis. Since the phase diagram tells the composition at equilibrium, phase diagrams are widely used to design reactions. On the other hand, it is necessary to reduce the number of variables by projecting a multi-dimensional complex system onto a certain surface to improve readability.



## 1-4-2 Kinetics of the synthesis reaction of solid-state materials

In the solid-state reaction, several models assuming either nucleation, geometrical contraction, diffusion, or reaction order as rate-limiting processes have been employed to rationalize the solid-state kinetics. These reaction models describe the reaction assuming different mechanisms. Nucleation presumes that the formation and growth of nuclei restrict the reaction. Geometrical contraction deals with the progress of the product layer and is affected by the morphologies. Diffusion assumes that the diffusion of consistent elements to the reaction sites governs the reaction limit. Reaction order describes the reaction in the same way as a homogenous system.

Table 1-1 lineup the reaction rate equation of proposed models by A. khawam and D. Flanagan<sup>[36]</sup>.

Table 1-1 Solid-State Rate Expressions for Different Reaction Models

Model	Differential Form <sup>a</sup> $f(\alpha) = \frac{1}{k} \frac{d\alpha}{dt}$	Integral Form <sup>a</sup> $g(\alpha) = kt$
<b>Nucleation models</b>		
Power law (P2)	$2 \alpha^{(1/2)}$	$\alpha^{(1/2)}$
Power law (P3)	$3 \alpha^{(2/3)}$	$\alpha^{(1/3)}$
Power law (P4)	$4 \alpha^{(3/4)}$	$\alpha^{(1/4)}$
Avrami-Erofe'ev (A2)	$2(1-\alpha)[- \ln(1-\alpha)]^{1/2}$	$[- \ln(1-\alpha)]^{1/2}$
Avrami-Erofe'ev (A3)	$3(1-\alpha)[- \ln(1-\alpha)]^{2/3}$	$[- \ln(1-\alpha)]^{1/3}$
Avrami-Erofe'ev (A4)	$4(1-\alpha)[- \ln(1-\alpha)]^{3/4}$	$[- \ln(1-\alpha)]^{1/4}$
Prout-Tompkins (B1)	$\alpha (1-\alpha)$	$\ln[\alpha/(1-\alpha)]$
<b>Geometrical Contraction models</b>		
Contracting area (R2)	$2(1-\alpha)^{1/2}$	$[1-(1-\alpha)^{1/2}]$
Contracting volume (R3)	$3(1-\alpha)^{2/3}$	$[1-(1-\alpha)^{1/3}]$
<b>Diffusion models</b>		
1-D diffusion (D1)	$1/2\alpha$	$\alpha^2$
2-D diffusion (D2)	$[- \ln(1-\alpha)]^{-1}$	$[(1-\alpha)\ln(1-\alpha)] + \alpha$
3-D diffusion-Jander eqn.(D3)	$3(1-\alpha)^{2/3}/2(1-(1-\alpha)^{1/3})$	$[1-(1-\alpha)^{1/3}]^2$
Ginstling-Brounshtein (D4)	$(3/2)((1-\alpha)^{-1/3}-1)$	$1-(2\alpha/3)-(1-\alpha)^{2/3}$
<b>Reaction-order models</b>		
Zero-order (F0/R1)	$1$	$\alpha$
First-order (F1)	$(1-\alpha)$	$- \ln(1-\alpha)$
Second-order (F2)	$(1-\alpha)^2$	$(1-\alpha)^{-1}-1$
Third-order (F3)	$(1-\alpha)^3$	$0.5 ((1-\alpha)^{-2}-1)$

<sup>a</sup>In some references  $f(\alpha)$  and  $g(\alpha)$  have opposite designations.

Diffusion is often the rate-limiting step in the solid-state reaction. Although the constituent elements of the precursors must diffuse through the contact points between the powders for the reaction to proceed, the diffusion coefficient in the solid phase is about  $10^{-10}$  cm<sup>2</sup>/s, which is lower than that in

the liquid phase ( $10^{-5}$  cm<sup>2</sup>/s) and the gas phase ( $10^{-1}$  cm<sup>2</sup>/s) by more than five orders of magnitude. Due to the slow atomic diffusion in the solid phase, sufficient diffusion of each element is often achieved using high-temperature heating since the diffusion coefficient in the solid phase depends on the temperature.

### **1-5 In-situ X-ray diffraction measurement to understand the synthesis reaction**

In recent years, in situ X-ray diffraction techniques have been used to quantitatively understand processes during reactions<sup>[37-45]</sup>. In-situ XRD can visualize the phase evolution of crystalline products depending on the time and temperature. Synchrotron XRD has been used due to the higher angle resolution, detection sensitivity, and response than conventional XRD which employed CuK $\alpha$  radiation. For example, the reaction of Y<sub>2</sub>O<sub>3</sub>, Ba(OH)<sub>2</sub>, and CuO oxide starting materials to produce the superconductor YBa<sub>2</sub>Cu<sub>3</sub>O<sub>7</sub> was investigated by using synchrotron diffraction. It was found that the reaction was primarily driven by thermodynamics and secondly kinetics including the formation of a liquid Ba-Cu-O phase governing the reaction<sup>[46]</sup>. A comparison of the reactions using elemental Fe, Si, S or Fe<sub>5</sub>S<sub>3</sub>, Fe<sub>3</sub>Si, S revealed that Fe<sub>2</sub>SiS<sub>4</sub> is formed quickly by circumventing the slow reaction between Si and S<sup>[43]</sup>.

### **1-6 Selection of materials**

MgCr<sub>2</sub>S<sub>4</sub> had attracted attention as a positive electrode material candidate for Mg secondary batteries<sup>[47, 48]</sup>, and Li<sub>3</sub>YCl<sub>6</sub> has been actively studied in recent years as one of the chloride solid electrolytes for all-solid-state Li secondary batteries<sup>[49, 50]</sup>.

### **1-7 Secondary battery materials**

The all-solid-state Li secondary batteries have advantages since replacing combustible organic

electrolytes with flame-retardant inorganic solid electrolytes improves the thermal stability of battery cells. Moreover, using a Li metal anode increases the specific capacity. In addition, oxide and chloride solid electrolytes are expected to be applied to the next-generation batteries, and the synthesis methods and properties of new electrolytes have been actively researched

#### **1-7-1 Ternary spinel sulfide $\text{MgCr}_2\text{S}_4$**

$\text{MgCr}_2\text{S}_4$  has been anticipated to have a high specific capacity ( $209 \text{ mA h g}^{-1}$ ) and energy density ( $244 \text{ W h kg}^{-1}$ ), a relatively low Mg ion diffusion barrier of 540 meV from first-principles calculations<sup>[51]</sup>, and was a candidate of cathode material for Mg ion batteries. It has been expected that Mg batteries can exhibit higher specific capacity than Li ones because the charge carrier is divalent Mg ions. The Mg metal cathode is also attractive since Mg is hardly deposited in a dendrite shape. Already, the intercalate and deintercalation of Mg in chevre sulfide  $\text{Mo}_6\text{S}_8$  and the operation of  $\text{Mo}_6\text{S}_8/\text{THF}/02-6 (\text{Mg}(\text{AlCl}_2\text{EtBu}_2)/\text{Mg}$  battery has been reported. The cubic  $\text{Ti}_2\text{S}_4$  spinel also has exhibited a capacity of 200 mAh using an organic electrolyte, APC/tetraglyme<sup>[52]</sup>. Since  $\text{MgCr}_2\text{S}_4$  is thermodynamically stable,  $\text{MgCr}_2\text{S}_4$  is successfully synthesized from elemental Mg, Cr, and S. Figure 1-2 shows the schematic image of the synthesis reaction of  $\text{MgCr}_2\text{S}_4$  reported by A. Wustrow *et al.* Nearly phase pure  $\text{MgCr}_2\text{S}_4$  was obtained using excess MgS and washing with acid. However, the synthesis of  $\text{MgCr}_2\text{S}_4$  took over one week since the reaction between MgS and  $\text{Cr}_2\text{S}_3$  is slow due to the small reaction enthalpy change even at 800 °C. Furthermore,  $\text{MgCr}_2\text{S}_4$  decomposes into MgS and  $\text{Cr}_2\text{S}_3$  when heated above 900 °C, suggesting that the reaction at a higher temperature will not yield a nearly single-phase product.

The synthesis and charge-discharge capability of  $\text{MgCr}_2\text{S}_4$  was been investigated whereas the recent studies on the charge reaction of  $\text{MgCr}_2\text{S}_4$  revealed that  $\text{MgCr}_2\text{S}_4$  does not exhibit charge capacity due to framework instability.

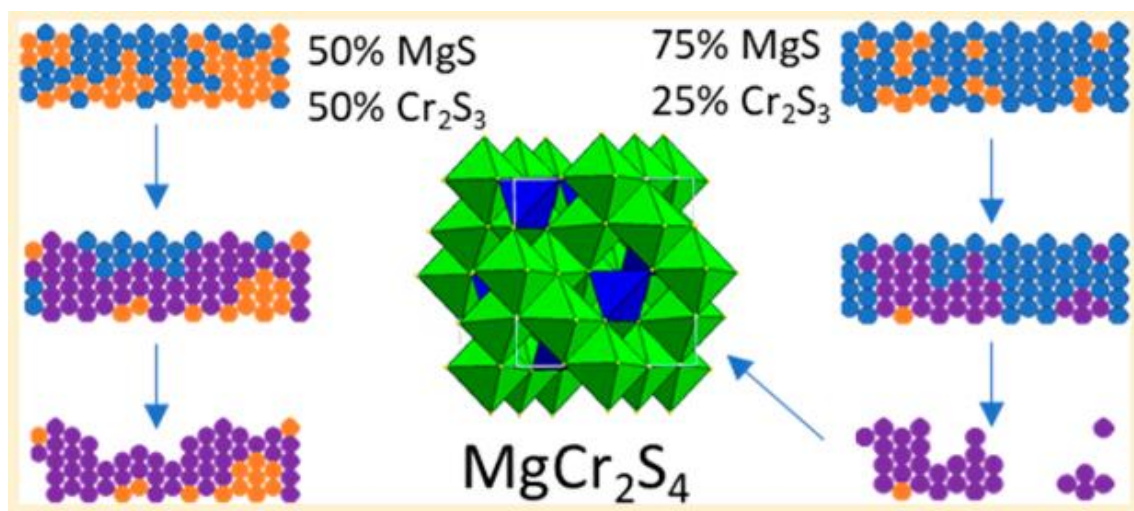


Figure 1-2: Schematic image of the synthesis reaction of  $\text{MgCr}_2\text{S}_4$  from the mixture of  $\text{MgS}$  and  $\text{Cr}_2\text{S}_3$  reported by A. Wustrow *et al.*

### 1-7-2 Ternary chloride $\text{Li}_3\text{MCl}_6$ (M=trivalent element)

$\text{Li}_3\text{YCl}_6$  has been attracting attention as a chloride solid electrolyte for all-solid-state Li batteries since it showed a high Li ion conductivity of about  $1 \text{ mS cm}^{-1}$ . Figure 1-3 shows the structures and ionic conductivity of ternary chlorides made by X. Li *et al.*<sup>[53]</sup>. This figure depicts the variety of structures of chlorides. The all-solid-state battery using  $\text{Li}_3\text{YCl}_6$ , and  $\text{LiCoO}_2$  as the cathode active material and Li-In alloy anode have been reported to operate for 100 cycles<sup>[49]</sup>.  $\text{Li}_3\text{YCl}_6$  is synthesized by planetary ball milling or high-temperature heating of a mixture of  $3\text{LiCl}$  and  $\text{YCl}_3$ , and crystalline samples with slightly different structures are obtained depending on the synthesis conditions<sup>[50]</sup>.  $\text{Li}_3\text{YCl}_6$  is crystalized with a layered structure in which Li and Y partially occupy octahedral spaces in the hexagonal close-packed lattice formed by Cl. The stacking fault along the c-axis in  $\text{Li}_3\text{YCl}_6$  which was produced only by mixing has been revealed. Furthermore, the correlation between the atomic displacement of Li in the structure, the occupancy of Y, and the volume of the octahedron have been shown from neutron diffraction<sup>[50]</sup>. In this study, I assumed that synthesis using salts consisting

of low valent anions and cations including  $\text{Li}^+$  and  $\text{Cl}^-$  is expected to result in high diffusion rates due to weak Coulomb attraction. For example, it has been reported that the reaction between  $\text{AgCl}$  and layered  $\text{YCl}_3$  proceeds at temperatures below  $400^\circ\text{C}$ <sup>[54]</sup>.

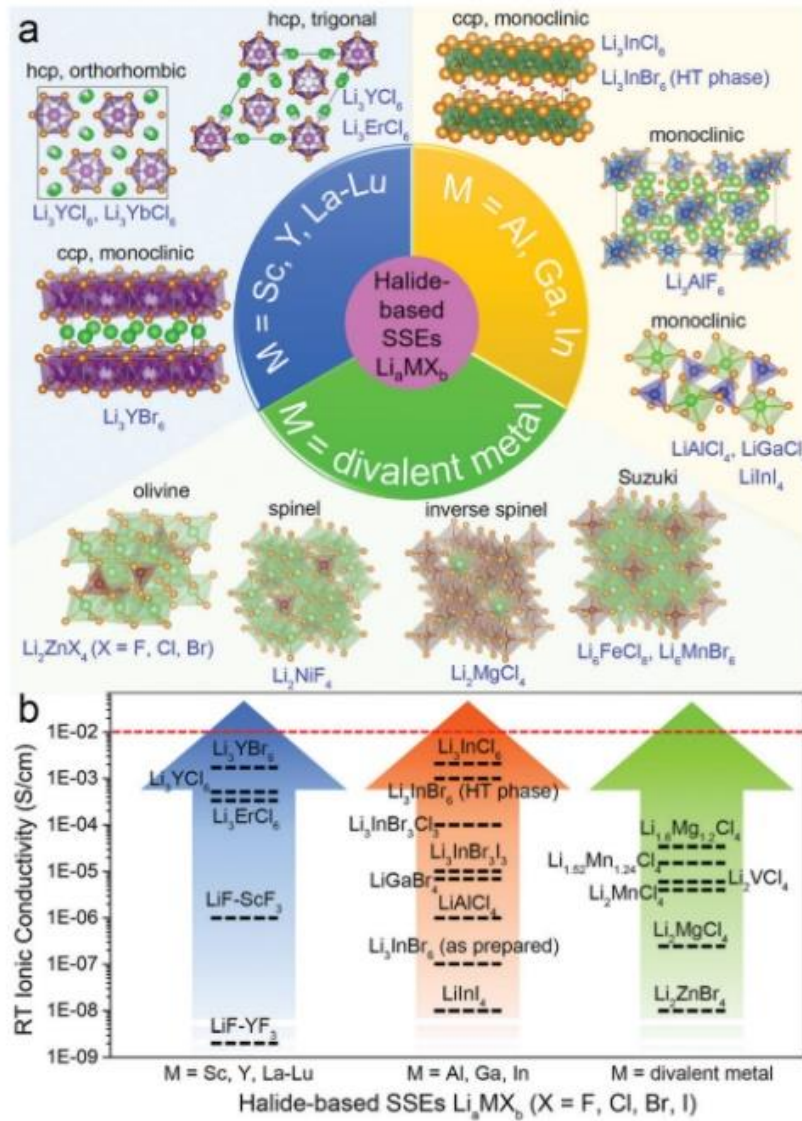


Figure 1-3: Structures and  $\text{Li}^+$  conductivities of ternary halide-based solid-electrolytes reported by X.

Li *et al.*

## 1-8 Aim and strategies of this work

In this study, I synthesized  $\text{MgCr}_2\text{S}_4$  and  $\text{Li}_3\text{YCl}_6$  at low temperatures and discussed their reactions. Specifically, I proposed two strategies to lower the reaction temperature; 1) the increase in the reaction enthalpy change using the metathesis reaction and the enhancement of the diffusion coefficient by the presence of the liquid phase for the synthesis of  $\text{MgCr}_2\text{S}_4$ , and 2) the weak Coulombic attraction between the anion,  $\text{Cl}^-$ , and cation,  $\text{Li}^+$ , in the starting materials of the solid-phase reaction, that leads to high diffusion rates and lowers the reaction temperature for  $\text{Li}_3\text{YCl}_6$ . The structure of this paper is shown below.

## 1-9 Contents of this paper

The second chapter reports the low-temperature synthesis of  $\text{MgCr}_2\text{S}_4$  by modifying the reaction process. In this study, the five-dimensional K-Mg-Cr-S-Cl phase diagram was transformed into a pseudo-three-dimensional  $\text{Na}_2\text{S-MgCl}_2\text{-CrCl}_3$  phase diagram by calculating the reaction enthalpy from the starting material to the product based on the first-principles calculation. Based on the projected quasi-ternary phase diagram, I focused on the synthesis of  $\text{MgCr}_2\text{S}_4$  using the metathesis reaction, in which ionic recombination occurs between the starting material and the product. The metathesis reaction of  $\text{MgCr}_2\text{S}_4$  adopted in this paper:  $2\text{NaCrS}_2 + \text{MgCl}_2 \rightarrow \text{MgCr}_2\text{S}_4 + 2\text{NaCl}$  has a  $\Delta H_{\text{rex}}$  of  $-47 \text{ kJ mol}^{-1}$ , which is a reaction enthalpy change compared to the solid-state reaction  $\text{MgS} + \text{Cr}_2\text{S}_3 \rightarrow \text{MgCr}_2\text{S}_4$  ( $-2 \text{ kJ/mol}$ ) is more than 20 times larger. Furthermore, by using molten salt, which is a liquid phase with a high diffusion rate, as a flux, the diffusion rate at low temperatures was improved, and the reaction rate was improved even at a low temperature of  $500^\circ\text{C}$  compared to the previous report that used heating for two weeks at  $800^\circ\text{C}$ . A novel low-temperature synthesis of  $\text{MgCr}_2\text{S}_4$  has become possible in as short a time as 30 minutes.

Chapter 3 reports the discovery of the novel polymorphs of  $\text{Li}_3\text{YCl}_6$  using the in-situ observation

method. In-situ XRD measurements revealed the existence of a novel polymorph of  $\text{Li}_3\text{YCl}_6$ , the average structures were determined by Rietveld analysis and the local structure was clarified by  $^7\text{Li}$  NMR and X-ray absorption. The occupancy of Y in the crystal structure and lattice volume of each polymorph changed slightly with synthesis. Furthermore, I clarified the changes in the surrounding environment of Li from the ionic conductivity obtained from the AC impedance method. Moreover, the reversibility of the phase transition reaction was confirmed by annealing the high-temperature phase.

Chapter 4 summarizes the types of metastability and determined the metastability of  $\text{Li}_3\text{MCl}_6$ . The type of reaction coordinates and designs to obtain metastable phases proposed so far are revisited. From the annealing of  $\text{Li}_3\text{YCl}_6$  shown in Chapter 3, it was clarified that the high-temperature phase of  $\text{Li}_3\text{YCl}_6$  with formula weight  $Z=3$  in the crystal structure is “remnant metastable” at ambient temperature.

Chapter 5 summarizes the low-temperature syntheses of  $\text{MgCr}_2\text{S}_4$  and  $\text{Li}_3\text{YCl}_6$  mentioned above, and emphasizes the importance of understanding thermodynamics and kinetics for lowering the temperature of material synthesis.

## 1-10 References

- [1] Hornbostel, M. D.; Hyer, E. J.; Thiel, J.; Johnson, D. C., *J. Am. Chem. Soc.*, 1997, **119**(11), 2665–
- [2] W. D. Kingery, H. K. Bowen, D. R. Uhlmann, Introduction to Ceramics, 2nd ed., *Wiley-Blackwell*, Hoboken, NJ, USA 1976.
- [3] M. G. Kanatzidis, K. R. Poeppelmeier, S. Bobev, A. M. Guloy, S.-J. Hwu, A. Lachgar, S. E. Latturmer, S. E. Raymond, D.-K. Seo, S. C. Sevov, A. Stein, B. Dabrowski, J. E. Greedan, M. Greenblatt, C. P. Grey, A. J. Jacobson, D. A. Keszler, J. Li, M. A. Subramanian, Y. Xia, T. Cagin, U. Häussermann, T. Hughbanks, S. D. Mahanti, D. Morgan, D.-K. Seo, N. A. Spaldin, W. E. Buhro, D. E. Giammar, J. A. Hollingsworth, D. C. Johnson, A. J. Nozik, X. Peng, R. L. Bedard, N. E. Brese, G. Cao, S. S. Dhingra, C. R. Kagan, D. B. Mitzi, M. J. Geselbracht, G. C. Lisensky, M. W. Lufaso, P. A. Maggard, O. K. Michael, A. P. Wilkinson, H.-C. zur Loye, T. Egami, J. E. Greedan, J. P. Hodges, J. D. Martin, J. B. Parise, B. H. Toby, T. A. Vanderah, P. C. Burns, J. Y. Chan, A. E. Meyer, C. B. Murray, A. P. Ramirez, M. D. Ward, L. Yu, M. A. Alario-Franco, P. D. Battle, T. Bein, C. L. Cahill, P. S. Halasyamani, A. Maignan, R. Seshadri, *Prog. Solid State Chem.* 2008, **36**, 1.
- [4] A. R. West, Solid State Chemistry and its Applications, *Wiley*, New York 2014.
- [5] Sun, W.; Dacek, S. T.; Ong, S. P.; Hautier, G.; Jain, A.; Richards, W. D.; Gamst, A. C.; Persson, K. A.; Ceder, G. *Sci. Adv.* 2016, **2**(11), e1600225.
- [6] Sleight, A. W., *Phys. Today*, 1991, **44**(6), 24–30.
- [7] Oike, H.; Kamitani, M.; Tokura, Y.; Kagawa, F., *Sci. Adv.*, 2018, **4**(10), 1–7.
- [8] Tan, X.; Geng, S.; Ji, Y.; Shao, Q.; Zhu, T.; Wang, P.; Li, Y.; Huang, X., *Adv. Mater.*, 2020, **32**(40), 1–7.
- [9] Cheetham, A. K. Advanced Inorganic Materials: An Open Horizon., *Science*, 1994, **264**(5160), 794–795.
- [10] Yao, Y.; Huang, Z.; Xie, P.; Lacey, S. D.; Jacob, R. J.; Xie, H.; Chen, F.; Nie, A.; Pu, T.; Rehwoldt,



- M.; Yu, D.; Zachariah, M. R.; Wang, C.; Shahbazian-Yassar, R.; Li, J.; Hu, L., *Science*, 2018, **359**(6383), 1489–1494.
- [11] Tatsumisago, M.; Shinkuma, Y.; Minami, T., *Nature*, 1991, **354**(6350), 217–218.
- [12] Kaup, K.; Zhou, L.; Huq, A.; Nazar, L. F., *J. Mater. Chem. A*, 2020, **8**(25), 12446–12456.
- [13] Kanazawa, K.; Yubuchi, S.; Hotehama, C.; Otoyama, M.; Shimono, S.; Ishibashi, H.; Kubota, Y.; Sakuda, A.; Hayashi, A.; Tatsumisago, M., *Inorg. Chem.*, 2018, **57**(16), 9925–9930.
- [14] Esters, M.; Alemayehu, M. B.; Jones, Z.; Nguyen, N. T.; Anderson, M. D.; Grosse, C.; Fischer, S. F.; Johnson, D. C., *Angew. Chemie Int. Ed.*, 2015, **54** (4), 1130–1134.
- [15] Hasegawa, T.; Kim, S. W.; Abe, Y.; Muto, M.; Watanabe, M.; Kaneko, T.; Uematsu, K.; Ishigaki, T.; Toda, K.; Sato, M.; Koide, J.; Toda, M.; Kudo, Y., *RSC Adv.*, 2017, **7**(40), 25089–25094.
- [16] Watanabe, M.; Inoi, J.; Kim, S. W.; Kaneko, T.; Toda, A.; Sato, M.; Uematsu, K.; Toda, K.; Koide, J.; Toda, M.; Kawakami, E.; Kudo, Y.; Masaki, T.; Yoon, D. H., *J. Ceram. Soc. Japan*, 2017, **125**(6), 472–475.
- [17] Kozawa, T.; Yanagisawa, K.; Suzuki, Y., *J. Ceram. Soc. Japan*, 2013, **121**(1411), 308–312.
- [18] Kashyap, A.; Singh, N. K.; Soni, M.; Soni, A. Chapter 3 - Deposition of Thin Films by Chemical Solution-Assisted Techniques; Das, S., Dhara, S. B. T.-C. S. S. for M. D. and T. F. D. A., Eds.; *Elsevier*, 2021; pp 79–117.
- [19] Walton, R. I., *Prog. Cryst. Growth Charact. Mater.*, 2011, **57**(4), 93–108.
- [20] Ohtomo, T.; Hayashi, A.; Tatsumisago, M.; Tsuchida, Y.; Hama, S.; Kawamoto, K., *J. Power Sources*, 2013, **233**, 231–235.
- [21] Dietrich, C.; Weber, D. A.; Sedlmaier, S. J.; Indris, S.; Culver, S. P.; Walter, D.; Janek, J.; Zeier, W. G., *J. Mater. Chem. A*, 2017, **5**(34), 18111–18119.
- [22] Hayashi, A.; Minami, K.; Ujiie, S.; Tatsumisago, M., *J. Non. Cryst. Solids*, 2010, **356**(44–49), 2670–2673.

- [23] Meyer, H.-J., *Dalt. Trans.*, 2010, **39**(26), 5973.
- [24] Treece, R. E.; Gillan, E. G.; Kaner, R. B., *Comments Inorg. Chem.*, 1995, **16**(6), 313–337.
- [25] Wiley, J. B.; Gillan, E. G.; Kaner, R. B., *Mater. Res. Bull.*, 1993, **28**(9), 893–900.
- [26] Odahara, J.; Sun, W.; Miura, A.; Rosero-Navarro, N. C.; Nagao, M.; Tanaka, I.; Ceder, G.; Tadanaga, K., *ACS Mater. Lett.*, 2019, **1**(1), 64–70.
- [27] Sakai, H.; Hirai, S.; Nagao, M.; Rosero-Navarro, N. C.; Miura, A.; Tadanaga, K., *J. Alloys Compd.*, 2022, **935**, 167986.
- [28] Bonneau, P. R.; Jarvis, R. F.; Kaner, R. B., *Nature*, 1991, **349**(6309), 510–512.
- [29] Yang, L. F.; Cao, M. L.; Cui, Y.; Wu, J. J.; Ye, B. H., *Cryst. Growth Des.* 2010, **10**(3), 1263–1268.
- [30] Krummacher, J.; Passerini, S.; Balducci, A., *Solid State Ionics*, 2015, **280**, 37–43.
- [31] Bowmaker, G. A.; Hanna, J. V.; Skelton, B. W.; White, A. H., *Chem. Commun.*, 2009, **16**, 2168–2170.
- [32] Gopalakrishnan, J., *Chem. Mater.*, 1995, **7**(7), 1265–1275.
- [33] Liu, G.; Li, T.; Xing, Y.; Pan, W., *IOP Conf. Ser. Mater. Sci. Eng.*, 2019, **678**(1).
- [34] Kokal, I.; Somer, M.; Notten, P. H. L.; Hintzen, H. T., *Solid State Ionics*, 2011, **185**(1), 42–46.
- [35] Jansen, M., *Pure Appl. Chem.*, 2014, **86**(6), 883–898.
- [36] Khawam, A.; Flanagan, D. R., *J. Pharm. Sci.*, 2006, **95**(3), 472–498.
- [37] Miura, A.; Bartel, C. J.; Goto, Y.; Mizuguchi, Y.; Moriyoshi, C.; Kuroiwa, Y.; Wang, Y.; Yaguchi, T.; Shirai, M.; Nagao, M.; Rosero-Navarro, N. C.; Tadanaga, K.; Ceder, G.; Sun, W.; Rosero-Navarro, N. C.; Tadanaga, K.; Ceder, G.; Sun, W., *Adv. Mater.*, 2021, **33**(24), 2100312.
- [38] Haynes, A. S.; Stoumpos, C. C.; Chen, H.; Chica, D.; Kanatzidis, M. G., *J. Am. Chem. Soc.*, 2017, **139**(31), 10814–10821.
- [39] Bianchini, M.; Wang, J.; Clément, R. J.; Ouyang, B.; Xiao, P.; Kitchaev, D.; Shi, T.; Zhang, Y.; Wang, Y.; Kim, H.; Zhang, M.; Bai, J.; Wang, F.; Sun, W.; Ceder, G., *Nat. Mater.*, 2020, **19**(10), 1088–

1095.

- [40] He, H.; Yee, C.-H. H.; McNally, D. E.; Simonson, J. W.; Zellman, S.; Klemm, M.; Kamenov, P.; Geschwind, G.; Zebro, A.; Ghose, S.; Bai, J.; Dooryhee, E.; Kotliar, G.; Aronson, M. C., *Proc. Natl. Acad. Sci. U. S. A.*, 2018, **115**(31), 7890–7895.
- [41] Kohlmann, H., *Eur. J. Inorg. Chem.*, 2019, **2019**(39–40), 4174–4180.
- [42] Nielsen, M. H.; Aloni, S.; De Yoreo, J. J., *Science*, 2014, **345**(6201), 1158–1162.
- [43] Jiang, Z.; Ramanathan, A.; Shoemaker, D. P., *J. Mater. Chem. C*, 2017, **5**(23), 5709–5717.
- [44] Martinolich, A. J.; Kurzman, J. A.; Neilson, J. R., *J. Am. Chem. Soc.*, 2016, **138**(34), 11031–11037.
- [45] Kamm, G. E.; Huang, G.; Vornholt, S. M.; McAuliffe, R. D.; Veith, G. M.; Thornton, K. S.; Chapman, K. W., *J. Am. Chem. Soc.* 2022, **144**(27), 11975–11979.
- [46] Miura, A.; Bartel, C. J.; Goto, Y.; Mizuguchi, Y.; Moriyoshi, C.; Kuroiwa, Y.; Wang, Y.; Yaguchi, T.; Shirai, M.; Nagao, M.; Rosero-Navarro, N. C.; Tadanaga, K.; Ceder, G.; Sun, W., *Adv. Mater.* 2021, **33**(24), 2100312.
- [47] Wustrow, A.; Key, B.; Phillips, P. J.; Sa, N.; Lipton, A. S.; Klie, R. F.; Vaughey, J. T.; Poeppelmeier, K. R., *Inorg. Chem.*, 2018, **57**(14), 8634–8638.
- [48] Caggiu, L.; Enzo, S.; Stievano, L.; Berthelot, R.; Gerbaldi, C.; Falco, M.; Garroni, S.; Mulas, G., *Batteries*, 2020, **6**(3), 43.
- [49] Asano, T.; Sakai, A.; Ouchi, S.; Sakaida, M.; Miyazaki, A.; Hasegawa, S., *Adv. Mater.*, 2018, **30**(44), 1803075.
- [50] Schlem, R.; Banik, A.; Ohno, S.; Suard, E.; Zeier, W. G., *Chem. Mater.*, 2021, **33**(1), 327–337.
- [51] Liu, M.; Jain, A.; Rong, Z.; Qu, X.; Canepa, P.; Malik, R.; Ceder, G.; Persson, K. A., *Energy Environ. Sci.*, 2016, **9**(10), 3201–3209.
- [52] Tao, Z. L.; Xu, L. N.; Gou, X. L.; Chen, J.; Yuan, H. T., *Chem. Commun.*, 2004, **18**, 2080–2081.

- [53] Li, X.; Liang, J.; Yang, X.; Adair, K. R.; Wang, C.; Zhao, F.; Sun, X., *Energy Environ. Sci.*, 2020, **13**(5), 1429–1461.
- [54] Steiner, H. -J; Lutz, H. D., *ZAAC J. Inorg. Gen. Chem.*, 1992, **613**(7), 26–30.

## Chapter 2 Low-temperature synthesis of $\text{MgCr}_2\text{S}_4$

### 2-1 Problems of high-temperature synthesis

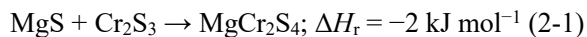
Synthesis is the bedrock of inorganic materials chemistry<sup>[1]</sup>, serving as the first step to any further investigation into the structure-property relationships of materials. For ceramic materials, the traditional approach to solid-state synthesis involves grinding or milling precursors into powder form, followed by the firing of these precursors at high temperatures to form more complex materials. While this approach has led to the synthesis of many inorganic materials, it remains limited by many thermodynamic and kinetic constraints<sup>[2]</sup>. For example, the synthesis temperature should be high enough to facilitate fast diffusion and reaction kinetics, but low enough that the target compound does not melt or decompose. However, high temperatures also lead to the ripening of large particles, which eliminates interfaces and thereby reduces reaction kinetics<sup>[3]</sup>. Because of these often conflicting constraints, solid-state synthesis occasionally proceeds with slow reaction kinetics, non-equilibrium intermediates, or impurities<sup>[4-6]</sup>, which hinder the phase-pure synthesis of the desired target material.

### 2-2 Synthesis and properties of $\text{MgCr}_2\text{S}_4$

One such material that has proven difficult to synthesize via traditional solid-state synthesis is  $\text{MgCr}_2\text{S}_4$  thiospinel. In the search for Mg-ion cathode materials beyond the dominant Chevrel  $\text{Mo}_6\text{S}_8$  phase<sup>[7]</sup>, Mg-thiospinels emerged as a promising class of compounds. Thiospinels benefit from a soft sulfur anion sublattice, which enhances Mg-ion mobility compared to oxides, and a spinel framework, which provides a favorable tetrahedral  $\rightarrow$  octahedral  $\rightarrow$  tetrahedral  $\text{Mg}^{2+}$  migration path with a low diffusion barrier<sup>[8, 9]</sup>.  $\text{MgTi}_2\text{S}_4$  was the first demonstrated Mg-thiospinel cathode material, successfully cycled at a C/5 rate at 60 °C and achieving a specific energy density of 230 W h kg<sup>-1</sup><sup>[1, 10, 11]</sup>. M. Liu *et al.* reported the computational search for other candidate Mg-thiospinels found  $\text{MgCr}_2\text{S}_4$  to possess compelling properties, including a high specific capacity (209 mA h g<sup>-1</sup>) and energy density (244 W

h kg<sup>-1</sup>), as well as a relatively low Mg-ion diffusion barrier of 540 meV<sup>[10]</sup>. Notably, MgCr<sub>2</sub>S<sub>4</sub> was calculated with density functional theory (DFT) to fall upon the Mg–Cr–S convex hull, meaning it is thermodynamically stable concerning competing compounds and should therefore be synthesizable.

Following this prediction, Wustrow *et al.* successfully synthesized MgCr<sub>2</sub>S<sub>4</sub> through a traditional solid-state synthesis approach—although it was found to be a laborious reaction<sup>[12]</sup>. Starting from elemental (Mg + Cr + S) precursors, the binary sulfides, MgS and Cr<sub>2</sub>S<sub>3</sub>, formed rapidly upon heating. However, the subsequent reaction from MgS + Cr<sub>2</sub>S<sub>3</sub> to ternary MgCr<sub>2</sub>S<sub>4</sub> required holding at 800 °C for two weeks, with numerous intermediate regrinds. Notably, the reaction could not be accelerated by carrying out the synthesis at higher temperatures as MgCr<sub>2</sub>S<sub>4</sub> decomposes into MgS and Cr<sub>2</sub>S<sub>3</sub> above 900 °C. Although MgCr<sub>2</sub>S<sub>4</sub> is indeed a thermodynamically stable compound, I calculate the driving force (reaction enthalpy,  $\Delta H_r$ ) for its formation from MgS + Cr<sub>2</sub>S<sub>3</sub> to be extremely small (–2 kJ mol<sup>-1</sup>, Eqn. (2-1)).



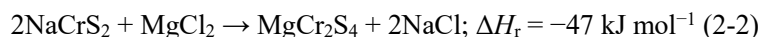
All reaction energies in this work utilize the publicly available DFT-calculated thermochemical data in the Materials Project database (Methods). The slow reaction kinetics observed by Wustrow *et al.* can be attributed to this small thermodynamic driving force. Moreover, long synthesis times can lead to the ripening of large MgCr<sub>2</sub>S<sub>4</sub> particles, which reduces the interfacial area needed to activate Mg-ion intercalation and further slows down the reaction kinetics.

### 2-3 Aim of this chapter

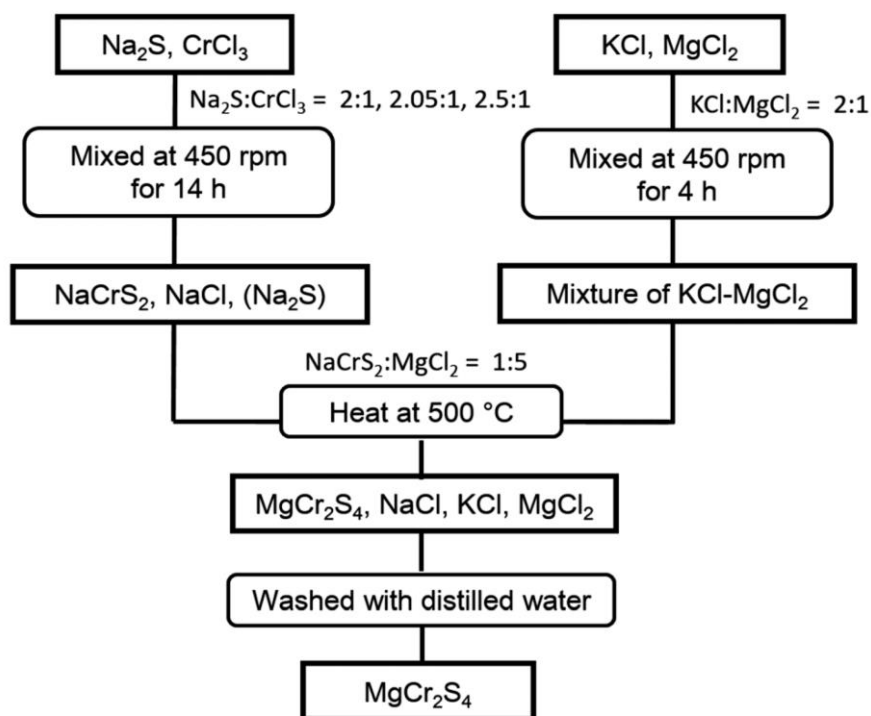
In this chapter, a new low-temperature synthesis of MgCr<sub>2</sub>S<sub>4</sub> is proposed. The effect of the increase in the reaction enthalpy change using the metathesis reaction and the enhancement of the diffusion coefficient by the presence of the liquid phase on the product were also discussed.

## 2-4 Metathesis reaction

Metathesis reactions offer an intriguing synthesis route to solid-state materials with otherwise small reaction energies. In a metathesis reaction, an alkali or alkaline earth metal compound is combined with a metal halide, which drives a highly exothermic double ion exchange reaction. For example, a compelling metathesis reaction for  $\text{MgCr}_2\text{S}_4$  can be written as:



The  $>20\times$  increase in thermodynamic driving force from  $\Delta H_r = -2 \text{ kJ mol}^{-1}$  to  $-47 \text{ kJ mol}^{-1}$  is because  $\text{Na}^+$  and  $\text{Cl}^-$  are separated in the precursors but rejoined to form the very stable NaCl salt on the product side. Along with a dramatic increase in reaction enthalpy, other advantages afforded by metathesis reactions include faster reaction kinetics and the potential to form nanocrystals and porous materials<sup>[13]</sup>. Not only can metathesis reactions be used to synthesize stable materials with otherwise small reaction energies, but the increased thermodynamic driving force and fast reaction kinetics also afford the synthesis of metastable materials<sup>[14]</sup>, as were previously demonstrated on nitrides<sup>[13, 15-17]</sup>, sulfides<sup>[13, 18, 19]</sup>, and oxides<sup>[20-22]</sup>. Motivated by the metathesis reaction shown in Eqn. (2-2), I designed a two-step sequential metathesis reaction to synthesize  $\text{MgCr}_2\text{S}_4$ , as visualized in Scheme 2-1.



Scheme 2-1: Two-step metathesis flux synthesis of  $\text{MgCr}_2\text{S}_4$ .

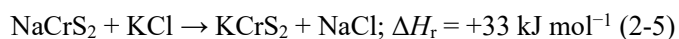
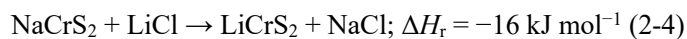
In the first reaction, I ball-milled  $\text{CrCl}_3$  and  $\text{Na}_2\text{S}$  to form  $\text{NaCrS}_2$  (Eqn. (2-3)). This reaction is highly exothermic ( $\Delta H_r = -359 \text{ kJ mol}^{-1}$ ) and proceeds even without external heating.



To conduct the metathesis reaction described in Eqn. (2-2), I next heated the byproducts from Eqn. (2-3) in a  $\text{KCl-MgCl}_2$  flux at  $500^\circ\text{C}$  in a nitrogen atmosphere. I prepared the  $\text{KCl-MgCl}_2$  flux at the eutectic composition of  $\text{KCl:MgCl}_2 = 2:1$ , which has a melting point of  $\sim 430^\circ\text{C}^{[23]}$ . I chose to conduct the reaction in a mixed chloride flux media because the eutectic temperature of a mixed chloride flux can be relatively low, which provides a liquid reaction media to facilitate fast diffusion kinetics. Here, I considered  $\text{LiCl}$ ,  $\text{NaCl}$ , and  $\text{KCl}$  as candidate flux chemistries to mix with  $\text{MgCl}_2$ . I disqualified a  $\text{LiCl-MgCl}_2$  flux because the ion-exchange reaction of  $\text{NaCrS}_2$  with  $\text{LiCl}$  has a favorable driving force to form  $\text{LiCrS}_2$ , which could compete with the formation of  $\text{MgCr}_2\text{S}_4$  (Eqn. (2-4)). I also disqualified  $\text{NaCl-MgCl}_2$  as a potential flux media because  $\text{NaCl}$  is a byproduct of the metathesis



reaction, meaning the NaCl composition of the flux would change as the metathesis reaction proceeds. Any deviation away from the eutectic composition would increase the melting temperature of the NaCl–MgCl<sub>2</sub> flux; which, if increased too much, could cause the flux to solidify and thereby disrupt the reaction. KCl–MgCl<sub>2</sub> emerges as the ideal flux media, because the formation of KCrS<sub>2</sub> from NaCrS<sub>2</sub> + KCl is not thermodynamically favorable (Eqn. (2-5)), and the eutectic point of KCl–MgCl<sub>2</sub> (~430 °C) is lower than that of NaCl–MgCl<sub>2</sub> (~445 °C)<sup>[24]</sup>. Furthermore, the formation of NaCl byproduct in a KCl–MgCl<sub>2</sub> flux would lower the KCl–MgCl<sub>2</sub> eutectic temperature<sup>[24]</sup>, and thereby would not impede the flux-mediated reaction kinetics.



These reaction thermodynamics are also straightforward to evaluate using the Materials Project Reaction Calculator app, which can help guide the rational design of flux chemistries.

## 2-5 Experimental

I synthesized NaCrS<sub>2</sub> in a reaction between CrCl<sub>3</sub> and Na<sub>2</sub>S by ball-milling at 450 rpm in a zirconia jar with zirconia milling media. I tried three molar ratios for CrCl<sub>3</sub> : Na<sub>2</sub>S = 1 : 2 (stoichiometric), 1 : 2.05 (2.5% Na<sub>2</sub>S excess), and 1 : 2.5 (25% Na<sub>2</sub>S excess) producing NaCrS<sub>2</sub> and NaCl (Eqn. (2-3)). In the second step, the ball-milled mixture of NaCrS<sub>2</sub> and NaCl was placed in a carbon crucible together with the MgCl<sub>2</sub>–KCl flux at a molar ratio of NaCrS<sub>2</sub> : MgCl<sub>2</sub> = 1 : 5. The phase diagram of MgCl<sub>2</sub>–KCl is shown as figure 2-1. The reaction was performed at 500 °C for 30 minutes in an inert nitrogen atmosphere. After cooling, the synthesized products were washed with distilled water and centrifuged in the air to remove the flux and excess MgCl<sub>2</sub> and Na<sub>2</sub>S.

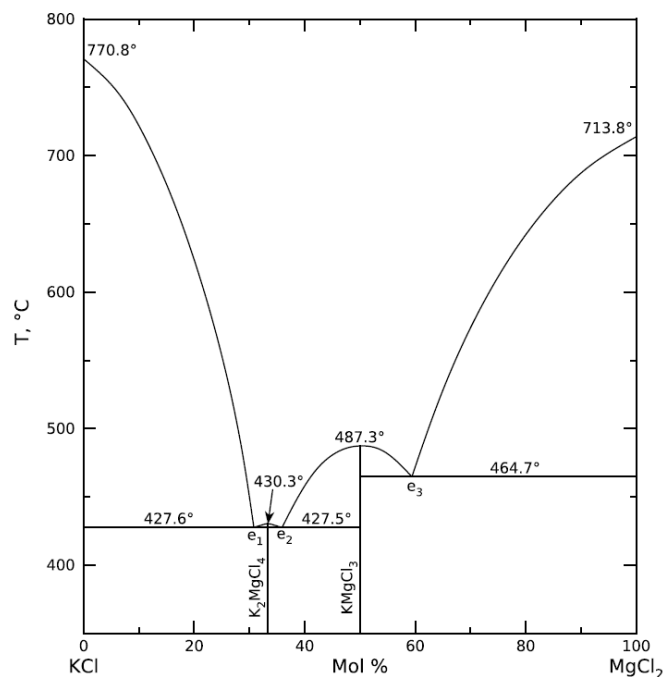


Figure 2-1: phase diagrams of KCl-  $\text{MgCl}_2$ . The molar ratio was determined to obtain the liquid phase at 500 °C.

The thermodynamics for all reactions discussed in this work are obtained from density functional theory calculations of the reaction enthalpy,  $\Delta H_r$ , as calculated using the Reaction Calculator app on the Materials Project database<sup>[25]</sup>. The deviation between calculated and experimentally obtained  $\Delta H_r$  for solid-state reactions, such as those discussed in this work, is expected to be on the order of 5~10  $\text{kJ mol}^{-1}$ <sup>[26, 27]</sup>. I note that  $\Delta H$  calculations do not account for the effects of temperature and entropy on the free energies. For solid-state reactions, the  $T\Delta S$  contribution to the free energy is generally negligible when all products and reactants are solids. I demonstrated this by calculating the Gibbs energies of reaction,  $\Delta G_r$ , at 1000 K for each of the reactions in this work using the model described in ref. 28 (Table 2-1).  $\Delta H_r$  and  $\Delta G_r$  (1000 K) are  $-2$  and  $-9 \text{ kJ mol}^{-1}$ , respectively, for Eqn. (2-1), and  $-47$  and  $-50 \text{ kJ mol}^{-1}$  for Eqn. (2-2). The syntheses were performed by two-step metathesis reactions.

First, the reaction between  $\text{CrCl}_3$  (99%, Sigma-Aldrich) and  $\text{Na}_2\text{S}$  (Nagao & Co., Ltd) with the molar ratio of 1 : 2, 1 : 2.05 (2.5%  $\text{Na}_2\text{S}$  excess), and 1 : 2.5 (25%  $\text{Na}_2\text{S}$  excess) were performed to produce  $\text{NaCrS}_2$  and  $\text{NaCl}$ . This reaction was performed by ball-milling at 450 rpm with a zirconia pot and ball. The second step was the reaction of  $\text{NaCrS}_2$  with  $\text{MgCl}_2$ . This reaction was performed at 500 °C for 30 minutes in an inert atmosphere. The ball-milled mixture of  $\text{NaCrS}_2$  and  $\text{NaCl}$  was placed in a carbon crucible together with an  $\text{MgCl}_2$ – $\text{KCl}$  flux:  $\text{MgCl}_2$  (99.9%, Kojundo Chemical Laboratory),  $\text{KCl}$  (>99.5%, Wako Chemicals). The molar ratio of  $\text{NaCrS}_2$  to  $\text{MgCl}_2$  was 1 : 5. After cooling, the synthesized products were washed with distilled water and centrifuged in an ambient atmosphere to remove flux and excess  $\text{MgCl}_2$  and  $\text{Na}_2\text{S}$ . XRD diffraction was measured by MiniFlex 600 (Rigaku). The composition ratio was determined by EDX equipped with scanning electron microscopy (SEM: TM3030). Morphology was observed by scanning transmission electron microscopy (STEM: Hitachi HD-2000). The diffuse reflectance spectra of  $\text{MgCr}_2\text{S}_4$  were measured using a UV-vis spectrophotometer (JASCO V-750) at room temperature. Mott–Schottky plot measurements were conducted using an ALS760Es electrochemical analyzer (BAS) at room temperature. The electrochemical cell was made of Pyrex glass and was a three-electrode-type system using Pt wire and an  $\text{Ag}/\text{AgCl}$  electrode (in saturated  $\text{KCl}$  aqueous solution) as the counter and reference electrodes, respectively. The pH of the electrolyte solution was adjusted to be 7.0 by mixing  $\text{NaH}_2\text{PO}_4 \cdot 2\text{H}_2\text{O}$  (99.0–102.0%, Kanto Chemical) and  $\text{Na}_2\text{HPO}_4 \cdot 12\text{H}_2\text{O}$  (>99.0%, Kanto Chemical), while keeping the total phosphate concentration of 0.1 M.

Table 2-1. Comparing reaction enthalpies,  $\Delta H_r$ , with Gibbs energies of reaction at 1000 K,  $\Delta G_r(1000\text{ K})$ , for each reaction.

Eq	$\Delta H_r$ (kJ/mol)	$\Delta G_r(1000\text{ K})$ (kJ/mol)	Reaction
1	-2	-9	$\text{MgS} + \text{Cr}_2\text{S}_3 \rightarrow \text{MgCr}_2\text{S}_4$
2	-47	-50	$2\text{NaCrS}_2 + \text{MgCl}_2 \rightarrow \text{MgCr}_2\text{S}_4 + 2\text{NaCl}$
3	-359	-326	$\text{CrCl}_3 + 2\text{Na}_2\text{S} \rightarrow \text{NaCrS}_2 + 3\text{NaCl}$
4	-16	-5	$\text{NaCrS}_2 + \text{LiCl} \rightarrow \text{LiCrS}_2 + \text{NaCl}$
5	33	36	$\text{NaCrS}_2 + \text{KCl} \rightarrow \text{KCrS}_2 + \text{NaCl}$

## 2-6 Results

Fig. 2-2 shows the XRD characterization of the synthesis products. The ball-milling of  $\text{Na}_2\text{S}$  and  $\text{CrCl}_3$  indeed produced  $\text{NaCrS}_2$  with  $\text{NaCl}$  byproduct, as anticipated from Eqn. (2-3). The reaction of  $\text{NaCrS}_2 + \text{NaCl}$  in the  $\text{MgCl}_2$ - $\text{KCl}$  flux resulted in  $\text{MgCr}_2\text{S}_4$ ,  $\text{Cr}_2\text{S}_3$ , and  $\text{MgO}$ , where the ratios of these products varied with the  $\text{Na}_2\text{S}$  excess in the precursor (Fig. 2-2). For a stoichiometric ratio of  $\text{CrCl}_3:\text{Na}_2\text{S} = 1:2$ , I observed a coexistence of  $\text{Cr}_2\text{S}_3$  and  $\text{MgCr}_2\text{S}_4$ . When the excess  $\text{Na}_2\text{S}$  was included in the synthesis of  $\text{NaCrS}_2$  (Eqn. (2-3)), the  $\text{Cr}_2\text{S}_3$  impurity from the flux reaction is diminished. With 25%  $\text{Na}_2\text{S}$  excess, the reaction yields nearly phase-pure  $\text{MgCr}_2\text{S}_4$ .

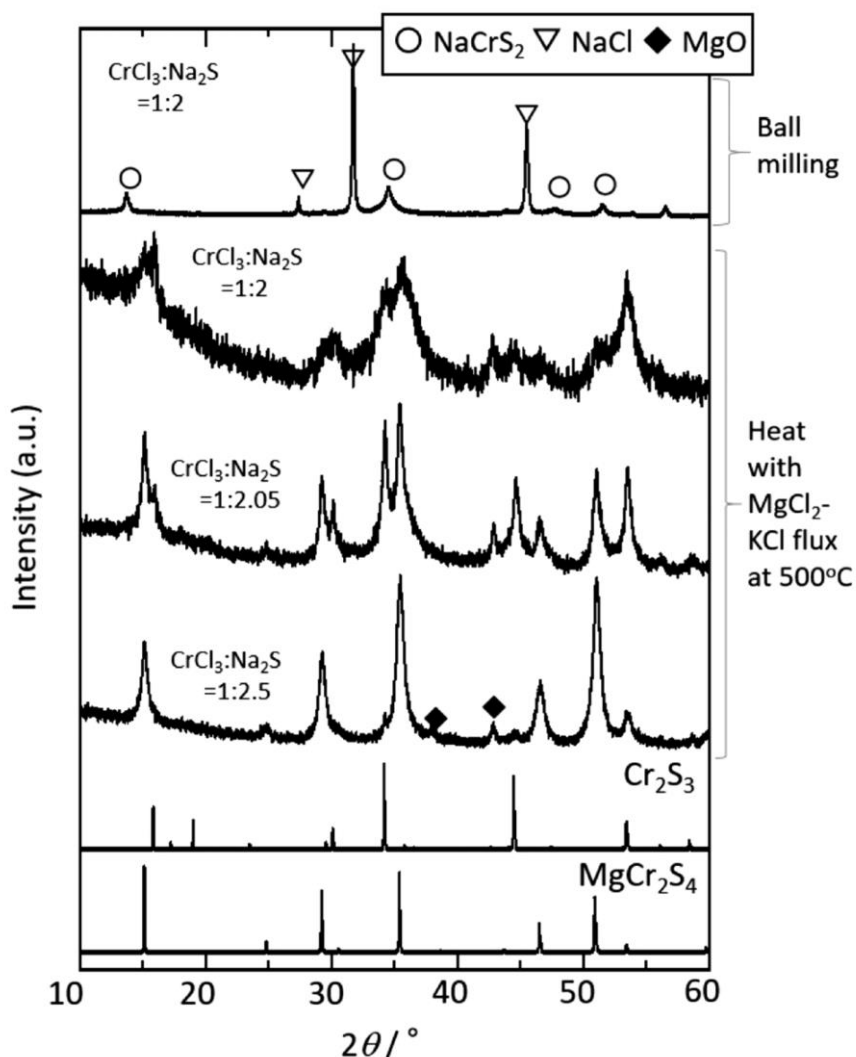


Fig. 2-2: XRD patterns of NaCrS<sub>2</sub> powder synthesized via ball milling from CrCl<sub>3</sub> and Na<sub>2</sub>S, and MgCr<sub>2</sub>S<sub>4</sub> powder synthesized by NaCrS<sub>2</sub> and MgCl<sub>2</sub>–KCl flux at 500 °C and subsequent wash with water. Different molar ratios of CrCl<sub>3</sub> : Na<sub>2</sub>S were utilized for producing MgCr<sub>2</sub>S<sub>4</sub>.

All metathesis byproducts and flux media (KCl, NaCl, MgCl<sub>2</sub>, Na<sub>2</sub>S) and any possibly synthesized MgS are soluble in water and were removed from the system by washing with distilled water. Although our final product yields MgCr<sub>2</sub>S<sub>4</sub> as the dominant phase, it contains MgO as a minor impurity. These reactions were conducted in an inert nitrogen atmosphere, suggesting the incorporation of oxygen in

MgO may have arisen from washing with water. To examine the effect of washing with water, I performed the same synthesis reaction of  $\text{NaCrS}_2$  with  $\text{MgBr}_2$ – $\text{KBr}$  flux, with excess  $\text{MgBr}_2$  and  $\text{Na}_2\text{S}$ , and subsequently removed metathesis products by washing with anhydrous methanol. In the  $\text{MgBr}_2$  synthesis, MgO still forms as an impurity phase, in fact with an even larger phase fraction than when synthesized in the  $\text{MgCl}_2$ – $\text{KCl}$  flux (Fig. 2-3).

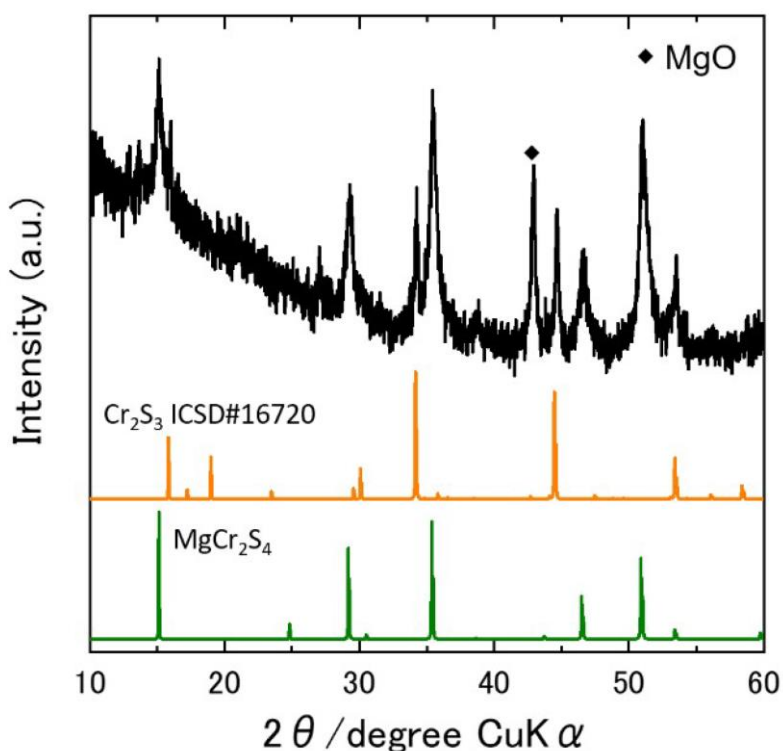


Figure 2-3: XRD patterns of  $\text{MgCr}_2\text{S}_4$  synthesized from  $\text{NaCrS}_2$  and  $\text{MgBr}_2$ – $\text{KBr}$  flux with excess  $\text{Na}_2\text{S}$  and subsequent washing with methanol.

This suggests that the oxygen does not originate from the water. Oxygen impurities may have therefore already existed in the  $\text{MgCl}_2$  or  $\text{MgBr}_2$  precursors, or from a low but nonzero  $p\text{O}_2$  and/or  $p\text{H}_2\text{O}$  in the nitrogen atmosphere.

I performed three control experiments to validate the importance of the designed synthesis parameters for the metathesis reaction of  $\text{MgCr}_2\text{S}_4$ . In our first control experiment, I reacted the traditional

precursors  $\text{MgS} + \text{Cr}_2\text{S}_3$  in the  $\text{MgCl}_2\text{--KCl}$  flux at  $500\text{ }^\circ\text{C}$  for 30 min, and in the second control experiment, I reacted  $\text{NaCrS}_2 + \text{MgCl}_2$  without the flux at  $500\text{ }^\circ\text{C}$  for 30 min. Neither of these two control experiments was found to form  $\text{MgCr}_2\text{S}_4$  (Fig. 2-4 and 2-5, respectively).

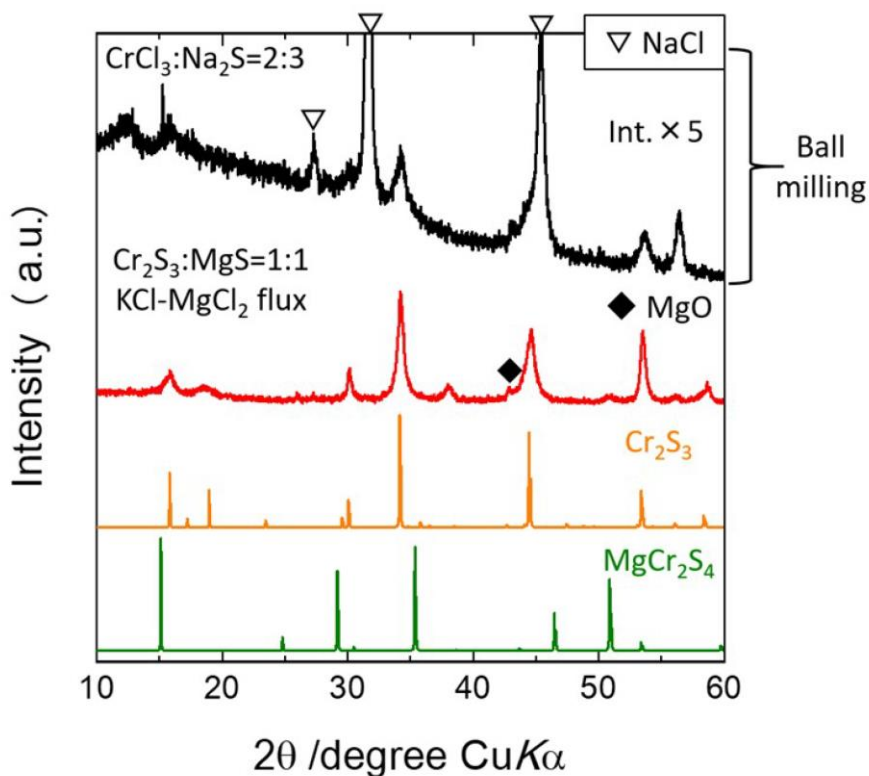


Figure 2-4: XRD patterns of (black) the mixture of  $\text{Cr}_2\text{S}_3$  and  $\text{NaCl}$  ball-milling of  $\text{CrCl}_3$  and  $\text{Na}_2\text{S}$  in the molar ratio of 2:3 according to  $2\text{CrCl}_3 + 3\text{Na}_2\text{S} \rightarrow \text{Cr}_2\text{S}_3 + 6\text{NaCl}$ , and (red) the product of the subsequent reaction between  $\text{Cr}_2\text{S}_3$  and  $\text{MgS}$  with  $\text{KCl-MgCl}_2$  flux at  $500\text{ }^\circ\text{C}$  for 30 min and wash with water. The product phase primarily shows  $\text{Cr}_2\text{S}_3$ , and no  $\text{MgCr}_2\text{S}_4$  is seen.

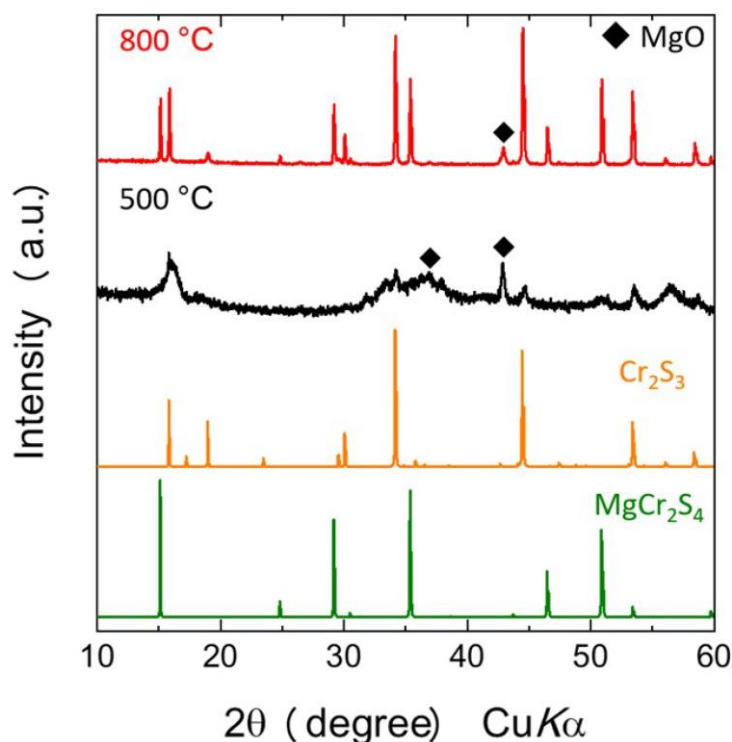


Figure 2-5: XRD pattern of the product of the reaction between  $\text{NaCrS}_2$  and  $\text{MgCl}_2$  without KCl at (black) 500 °C and (red) 800 °C for 30 min. No  $\text{Na}_2\text{S}$  excess was added. The reaction at 500 °C does not yield  $\text{MgCr}_2\text{S}_4$  peaks. The 800 °C sample does show  $\text{MgCr}_2\text{S}_4$  peaks, whose formation is likely facilitated by  $\text{MgCl}_2$  melting at 714°C<sup>[29]</sup>.

The former reaction supports the importance of metathesis precursors,  $\text{NaCrS}_2 + \text{MgCl}_2$ , while the latter reaction supports the need for a liquid phase (*i.e.*,  $\text{MgCl}_2$ –KCl flux). For the third control experiment, I reacted  $\text{NaCrS}_2$  with  $\text{MgCl}_2$  at 800 °C, where  $\text{MgCl}_2$  becomes liquid even without KCl (the melting point of  $\text{MgCl}_2$  is 714 °C). This reaction did form  $\text{MgCr}_2\text{S}_4$ , along with  $\text{Cr}_2\text{S}_3$  impurity (Fig. 2-5). This final control reaction shows that  $\text{MgCl}_2$  liquid is important for this reaction, and the presence of KCl enables this liquid phase to form well below the  $\text{MgCl}_2$  melting point, decreasing the required temperature from 714 °C to 430 °C. Together, these experiments show that the rapid synthesis of  $\text{MgCr}_2\text{S}_4$  at 500 °C requires the metathesis precursors ( $\text{NaCrS}_2 + \text{MgCl}_2$ ) and the  $\text{MgCl}_2$ –KCl flux.



The reaction process was also examined by in-situ synchrotron XRD. Fig 2-6a depicts the temperature dependence of peak intensities for the reaction. Peaks were colored blue to white according to their intensities. All peaks can be indexed as starting materials under 700 K and were not observed from 700 to 900 K, suggesting the melting of  $\text{MgCl}_2$ -KCl flux and dissolution of  $\text{NaCrS}_2$ ,  $\text{Na}_2\text{S}$ , and  $\text{NaCl}$ . The products crystallized under 700 K during the cooling down to 300 K. Fig 2-6b shows the XRD pattern of the sample after heating and cooling. Only the temperature sweep between 300 and 900 K at the sweep speed of 30 K/min produced  $\text{MgCr}_2\text{S}_4$ , indicating the importance of metathesis reaction and flux.

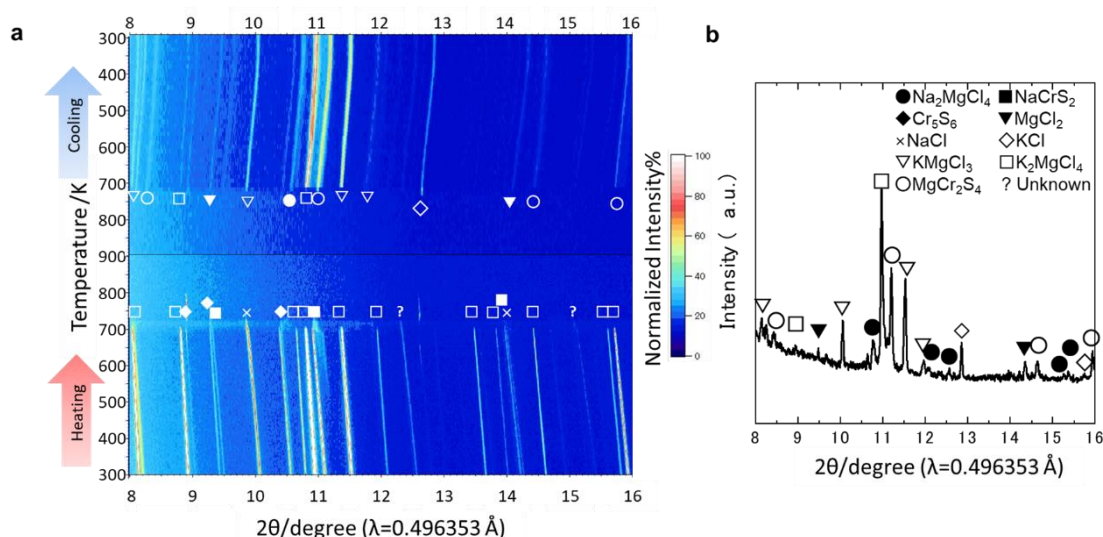


Figure 2-6: Synchrotron XRD measurement of reaction between  $\text{MgCl}_2$ -KCl flux and  $\text{NaCrS}_2$ . (a) in-situ XRD patterns during the reaction, and (b) XRD patterns of the same sample after cooling down to 300 K. The peaks were not observed over 700 K which corresponds to the melting point of the flux,  $\text{K}_2\text{MgCl}_4$ , suggesting the molten flux was the key for the reaction.

Rietveld refinement of  $\text{MgCr}_2\text{S}_4$  synthesized from  $\text{Na}_2\text{S}$  and  $\text{MgCl}_2$  excess (Fig. 2-7a) shows that the lattice parameter of  $\text{MgCr}_2\text{S}_4$  is 1.01426(12) nm, agreeing with the previously reported  $\text{MgCr}_2\text{S}_4$  synthesized by high-temperature solid-state synthesis (1.01415(2) nm)<sup>[12]</sup>. Rietveld refinement shows no inversion between Mg and Cr sites in the spinel structure. Fig. 2-7b shows the STEM images and corresponding EDX mapping of  $\text{MgCr}_2\text{S}_4$  particles synthesized via metathesis reactions with  $\text{Na}_2\text{S}$  and  $\text{MgCl}_2$  excess. The as-synthesized particles are 50–200 nm in size and 20–50 nm in thickness. The relative surface area of powder by  $\text{N}_2$  absorption is found to be  $55 \text{ m}^2 \text{ g}^{-1}$ . These small  $\text{MgCr}_2\text{S}_4$  particle sizes result from the low temperatures and short reaction times of metathesis synthesis, which quench the nanoparticles shortly after nucleation and before significant crystal growth occurs<sup>[13]</sup>. This can be contrasted against conventional solid-state synthesis, where high reaction temperatures and long anneal times tend to yield large particle sizes due to Ostwald ripening and particle coarsening during crystal growth<sup>[3, 30]</sup>. The molar ratio of Mg/Cr/S determined by EDX of the product is 1/2.4/4.1, which is close to the stoichiometric ratio of  $\text{MgCr}_2\text{S}_4$ . EDX mapping showed homogeneously distributed Mg and Cr, further supporting the formation of  $\text{MgCr}_2\text{S}_4$ .

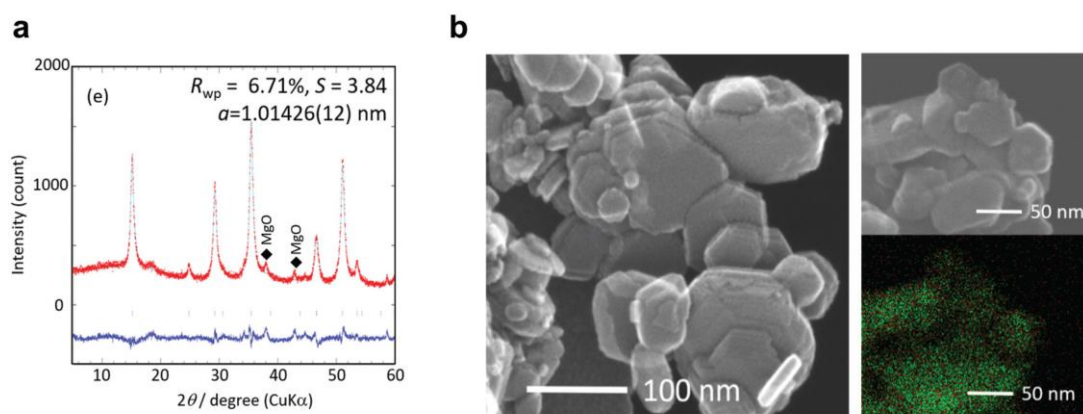


Fig. 2-7: (a) Rietveld profile of  $\text{MgCr}_2\text{S}_4$  synthesized with excess  $\text{Na}_2\text{S}$ . The residual is shown as the blue line. (b) STEM image of  $\text{MgCr}_2\text{S}_4$  platelet particles. The right side is STEM and EDX mapping: red and green signals represent Mg and Cr signals, respectively.

The electronic properties of  $\text{MgCr}_2\text{S}_4$  are an important consideration for Mg-ion battery performance and photochemical applications because  $\text{Cr}_2\text{S}_3$  has been reported as an n- and p-type semiconductor (band gap,  $E_g = 0.8 \text{ eV}$ )<sup>[31]</sup>. I measured the optical band gap of  $\text{MgCr}_2\text{S}_4$  using diffuse reflectance spectroscopy, which I estimate from the Tauc-plot to be 2.2 eV (Fig. 2-8). Using Mott–Schottky plot analysis (Fig. 2-9),  $\text{MgCr}_2\text{S}_4$  is shown to be an n-type semiconductor with a flat-band potential of ca.  $-0.6 \text{ V}$  vs.  $\text{Ag}/\text{AgCl}$  at pH 7.0, indicating it is also a candidate  $\text{H}_2$  evolution photocatalyst under visible light radiation<sup>[32]</sup>.

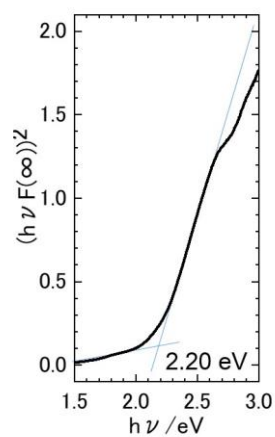


Figure 2-8: Tauc plot of  $\text{MgCr}_2\text{S}_4$  powders synthesized under  $\text{Na}_2\text{S}$  excess condition.

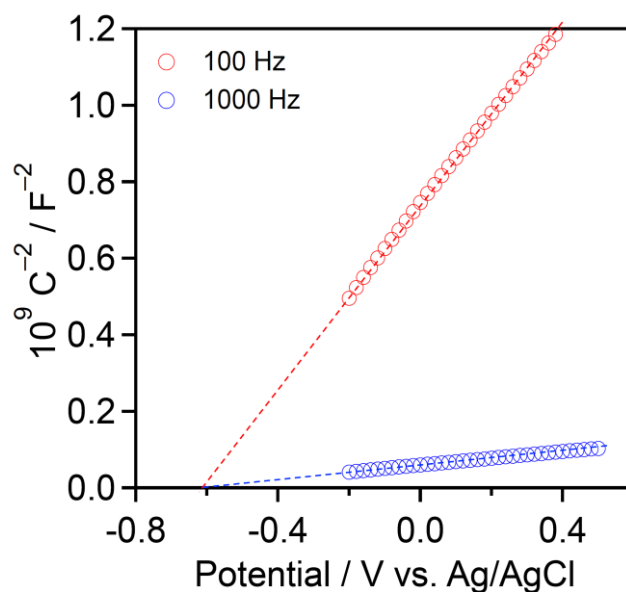


Figure 2-9: Mott-Schottky plot of the  $\text{MgCr}_2\text{S}_4/\text{FTO}$  electrode measured in aqueous  $\text{NaH}_2\text{PO}_4$ – $\text{Na}_2\text{HPO}_4$  solution ( $\text{PO}_4^{3-} = 0.1 \text{ M}$ ) at pH 7.0. The electrode was prepared by electrophoretic deposition in a 50 mL acetone solution (>99.5%, Kanto Chemical) containing 0.05 g  $\text{MgCr}_2\text{S}_4$  powder (synthesized under  $\text{Na}_2\text{S}$  excess condition) and 10 mg iodine (>99.8%, Wako Pure Chemicals). Two parallel FTO electrodes were immersed in the solution with ca. 15 mm separation, and a 20 V bias was applied between them for 30 s using a potentiostat (PSW 80-13.5, GW Instek). The  $\text{MgCr}_2\text{S}_4$ -coated area was fixed ca.  $1.5 \text{ cm} \times 3.5 \text{ cm}$ .

## 2-7 Discussion

The accelerated formation of  $\text{MgCr}_2\text{S}_4$  during metathesis (~30 minutes) compared with solid-state synthesis (~2 weeks) can be rationalized from the thermodynamic topology of each synthesis space. Fig. 2-10a shows the ternary convex hull phase diagram for Mg–Cr–S, and Fig. 2-10b shows a pseudo-ternary convex hull phase diagram for  $\text{MgCl}_2$ – $\text{CrCl}_3$ – $\text{Na}_2\text{S}$ , which is a slice of the larger five-component Mg–Cr–S–Na–Cl phase diagram. The color bar illustrates the ‘depth’ of the convex hull, corresponding to the reaction energy at each composition relative to the precursor endpoints. Even

though  $\text{MgCr}_2\text{S}_4$  has a very favorable formation enthalpy of  $-1.289 \text{ eV atom}^{-1}$ ,  $\text{MgS}$  and  $\text{Cr}_2\text{S}_3$  also have very negative formation enthalpies of  $-1.76$  and  $-1.097 \text{ eV atom}^{-1}$ , respectively. In the  $\text{Mg-Cr-S}$  phase diagram, the deepest point is at the  $\text{MgS}$  composition, meaning  $\text{MgS}$  acts as a thermodynamic ‘sink’ in the traditional ceramic synthesis and explains why  $\text{MgS}$  tends to persist during the traditional ceramic synthesis. Fig. 2-10c depicts the tiny energy gain to form  $\text{MgCr}_2\text{S}_4$  along the  $\text{MgS-Cr}_2\text{S}_3$  reaction tie-line, which further underlies the slow reaction kinetics.

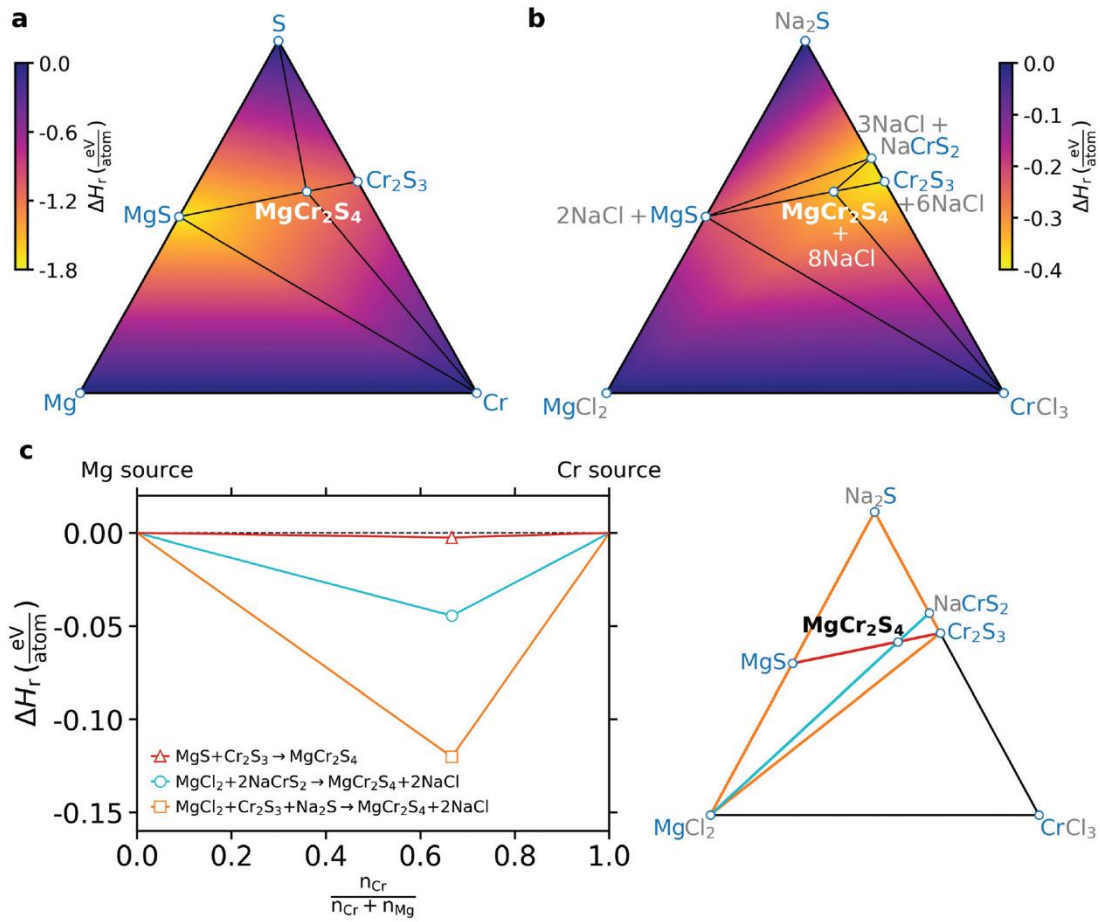


Fig. 2-10: Ternary phase diagrams for (a) Mg–Cr–S, corresponding to a traditional ceramic synthesis reaction, and (b)  $\text{MgCl}_2$ – $\text{CrCl}_3$ – $\text{Na}_2\text{S}$ , corresponding to a metathesis reaction. The color bar indicates the reaction enthalpy between the corners of each triangle and the convex hull, which represents the minimum energy phase or a mixture of phases at each composition. For (b),  $\Delta H_r$  is calculated by considering the formation of NaCl where appropriate and therefore is a pseudo-ternary representation of the quinary Mg–Cr–S–Na–Cl chemical space. (c) Driving force for  $\text{MgCr}_2\text{S}_4$  formation from three routes, highlighted by their color in the corresponding pseudo-ternary phase diagram. The reaction relevant to ceramic synthesis (Eqn. (2-1)) is shown in red, the metathesis reaction (Eqn. (2-3)) is shown in blue, and the reaction that proceeds with excess  $\text{Na}_2\text{S} + \text{MgCl}_2$ , and consumes impurity  $\text{Cr}_2\text{S}_3$ , is shown in orange.

On the other hand, the  $\text{MgCl}_2\text{--CrCl}_3\text{--Na}_2\text{S}$  metathesis phase diagram exhibits a qualitatively different thermodynamic topology. Here, each  $\text{Mg--Cr--S}$  composition must also be accompanied by a stoichiometrically balanced amount of  $\text{NaCl}$ , which modifies the reaction energies at each composition in the pseudo-ternary space.  $\text{MgCr}_2\text{S}_4$  is balanced by 8  $\text{NaCl}$ , whereas  $\text{MgS}$  is balanced by 2  $\text{NaCl}$ ,  $\text{NaCrS}_2$  by 3  $\text{NaCl}$ , and  $\text{Cr}_2\text{S}_3$  by 6  $\text{NaCl}$ . In the  $\text{MgCl}_2\text{--CrCl}_3\text{--Na}_2\text{S}$  phase diagram, the inclusion of  $\text{NaCl}$  shifts the deepest thermodynamic point from  $\text{MgS}$  to  $\text{MgCr}_2\text{S}_4 + \text{Cr}_2\text{S}_3$ , which are indeed the observed reaction products in Fig. 2-1 when synthesized without  $\text{Na}_2\text{S}$  excess. The metathesis route, therefore, enhances the selective synthesis of  $\text{MgCr}_2\text{S}_4$  by relocating the thermodynamic sink in composition space. Furthermore, because  $\text{S}$  is tied up with  $\text{Cr}$  in the  $\text{NaCrS}_2$  precursor,  $\text{MgS}$  is unlikely to form in the metathesis reaction, as this would require  $\text{NaCrS}_2$  decomposition and subsequent reaction of  $\text{S}$  with the  $\text{MgCl}_2$  flux.

By increasing the amount of  $\text{Na}_2\text{S}$  excess in the precursor, the diffraction peaks of  $\text{MgCr}_2\text{S}_4$  became dominant and the  $\text{Cr}_2\text{S}_3$  impurity is eliminated (Fig. 2-1). This can be rationalized from Le Chatelier's principle, as illustrated in Fig. 2-10c, where  $\text{Cr}_2\text{S}_3$  impurities react with excess  $\text{Na}_2\text{S}$  as well as excess  $\text{MgCl}_2$  from the flux, which further drives the reaction towards the  $\text{MgCr}_2\text{S}_4$  product side. The reaction between  $\text{Cr}_2\text{S}_3$ ,  $\text{MgCl}_2$ , and  $\text{Na}_2\text{S}$  (Fig. 2-10c, orange line) has a larger thermodynamic driving force than that between  $\text{NaCrS}_2$  and  $\text{MgCl}_2$  (Fig. 2-10c, blue line). Operating with excess  $\text{Na}_2\text{S}$  and  $\text{MgCl}_2$ , therefore, encourages the formation of  $\text{MgCr}_2\text{S}_4$  at the expense of the  $\text{Cr}_2\text{S}_3$  impurity. Wustrow *et al.* used a similar strategy in the traditional solid-state synthesis route, providing excess  $\text{MgS}$  to react with  $\text{Cr}_2\text{S}_3$  impurities to achieve high-purity  $\text{MgCr}_2\text{S}_4$ .

## 2-8 Conclusions

In summary, I demonstrated low-temperature metathesis reactions as a powerful synthesis route to inorganic materials with otherwise small thermodynamic driving forces. The formation of NaCl as a byproduct not only increases the reaction enthalpy of forming the target phase but shifts the topology of the phase diagram, changing the composition of the deepest point of the convex hull and thereby enhancing structure-selectivity. Here, I demonstrated the metathesis synthesis of  $\text{MgCr}_2\text{S}_4$  in only 30 minutes at 500 °C, in contrast to a two-week traditional ceramic synthesis at 800 °C with multiple intermediate regrinds. Furthermore, the synthesized  $\text{MgCr}_2\text{S}_4$  particles were 100–200 nm in size, which is a smaller particle size than would be realized in a direct solid-state ceramic synthesis. Thus, the metathesis synthesis of  $\text{MgCr}_2\text{S}_4$  enables future studies of its electrochemical performance for Mg-battery and photocatalytic applications.

From a more general perspective, the concept of the metathesis reaction broadens how we evaluate synthesis and synthesizability. Traditionally, I take an ‘addition’ approach to materials synthesis, where one mixes simple precursors to form a more complex multi-component material. In the metathesis route, the reactions are driven by stable but removable byproducts, which include but are not limited to alkali metal halides. For example, the reaction of chlorides/oxides with  $\text{H}_2\text{S}$  or  $\text{NH}_3$  gas could also be used to synthesize sulfides, oxysulfides, nitrides, and oxynitrides by generating  $\text{HCl}/\text{H}_2\text{O}$  gas as a byproduct<sup>[33-35]</sup>. The inclusion of these extra species into the phase diagram provides new degrees of freedom for synthesis design, opening up a vast and promising design space for clever metathesis reactions, which can be rapidly screened and evaluated using publicly available DFT thermochemical data. Creative new precursor combinations are still waiting to be exploited within a metathesis synthesis paradigm, which may currently be overlooked due to preconceived notions about precursor selection<sup>[36]</sup>.



## 2-9 References

- [1] M. G. Kanatzidis, K. R. Poeppelmeier, S. Bobev, A. M. Guloy, S.-J. Hwu, A. Lachgar, S. E. Latturmer, R. E. Schaak, D.-K. Seo, S. C. Sevov, A. Stein, B. Dabrowski, J. E. Greedan, M. Greenblatt, C. P. Grey, A. J. Jacobs<sup>1</sup> M. G. Kanatzidis, K. R. Poeppelmeier, S. Bobev, A. M. Guloy, S.-J. Hwu, A. Lachgar, S. E. Latturmer, R. E. Schaak, D.-K. Seo, S. C. Sevov, A. Stein, B. Dabrowski, J. E. Greedan, M. Greenblatt, C. P. Grey, A. J. Jacobson, D. A. Keszler, J. Li, M. A. Subramanian, Y. Xia, T. Cagin, U. Ha<sup>2</sup>ussermann, T. Hughbanks, S. D. Mahanti, D. Morgan, D.-K. Seo, N. A. Spaldin, W. E. Buhro, D. E. Giammar, J. A. Hollingsworth, D. C. Johnson, A. J. Nozik, X. Peng, R. L. Bedard, N. E. Brese, G. Cao, S. S. Dhingra, C. R. Kagan, D. B. Mitzi, M. J. Geselbracht, G. C. Lisensky, M. W. Lufaso, P. A. Maggard, O. K. Michael, A. P. Wilkinson, H.-C. zur Loye, T. Egami, J. E. Greedan, J. P. Hodges, J. D. Martin, J. B. Parise, B. H. Toby, T. A. Vanderah, P. C. Burns, J. Y. Chan, A. E. Meyer, C. B. Murray, A. P. Ramirez, M. D. Ward, L. Yu, M. A. Alario-Franco, P. D. Battle, T. Bein, C. L. Cahill, P. S. Halasyamani, A. Maignan and R. Seshadri, *Prog. Solid State Chem.*, 2008, **36**, 1–133.
- [2] F. J. DiSalvo, *Science*, 1990, **247**, 649–655.
- [3] R. M. German, in *Encyclopedia of Materials: Science and Technology*, ed. K. H. J. Buschow, R. W. Cahn, M. C. Flemings, B. Ilshner, E. J. Kramer, S. Mahajan and P. Veyssière, Elsevier, *Oxford*, 2001, pp. 8641–8643.
- [4] D. P. Shoemaker, Y.-J. Hu, D. Y. Chung, G. J. Halder, P. J. Chupas, L. Soderholm, J. F. Mitchell and M. G. Kanatzidis, *Proc. Natl. Acad. Sci. U. S. A.*, 2014, **111**, 10922.
- [5] Z. Jiang, A. Ramanathan, and D. P. Shoemaker, *J. Mater. Chem. C*, 2017, **5**, 5709–5717.
- [6] A. S. Haynes, C. C. Stoumpos, H. Chen, D. Chica and M. G. Kanatzidis, *J. Am. Chem. Soc.*, 2017, **139**, 10814–10821.
- [7] D. Aurbach, Z. Lu, A. Schechter, Y. Gofer, H. Gizbar, R. Turgeman, Y. Cohen, M. Moshkovich and E. Levi, *Nature*, 2000, **407**, 724–727.

- [8] Z. Rong, R. Malik, P. Canepa, G. Sai Gautam, M. Liu, A. Jain, K. Persson, and G. Ceder, *Chem. Mater.*, 2015, **27**, 6016–6021.
- [9] M. Liu, Z. Rong, R. Malik, P. Canepa, A. Jain, G. Ceder, and K. A. Persson, *Energy Environ. Sci.*, 2015, **8**, 964–974.
- [10] M. Liu, A. Jain, Z. Rong, X. Qu, P. Canepa, R. Malik, G. Ceder, and K. A. Persson, *Energy Environ. Sci.*, 2016, **9**, 3201–3209.
- [11] X. Sun, P. Bonnick, V. Duffort, M. Liu, Z. Rong, K. A. Persson, G. Ceder and L. F. Nazar, *Energy Environ. Sci.*, 2016, **9**, 2273–2277.
- [12] A. Wustrow, B. Key, P. J. Phillips, N. Sa, A. S. Lipton, R. F. Klie, J. T. Vaughey, and K. R. Poeppelmeier, *Inorg. Chem.*, 2018, **57**, 8634–8638.
- [13] J. B. Wiley and R. B. Kaner, *Science*, 1992, **255**, 1093–1097.
- [14] W. Sun, S. T. Dacek, S. P. Ong, G. Hautier, A. Jain, W. D. Richards, A. C. Gamst, K. A. Persson, and G. Ceder, *Sci. Adv.*, 2016, **2**, e1600225.
- [15] J. Odahara, W. Sun, A. Miura, N. C. Rosero-Navarro, M. Nagao, I. Tanaka, G. Ceder and K. Tadanaga, *ACS Mater. Lett.*, 2019, **1**, 64–70.
- [16] A. Miura, C. Rosero-Navarro, Y. Masubuchi, M. Higuchi, S. Kikkawa and K. Tadanaga, *Angew. Chem., Int. Ed.*, 2016, **55**, 7963–7967.
- [17] E. G. Rognerud, C. L. Rom, P. K. Todd, N. R. Singstock, C. J. Bartel, A. M. Holder and J. R. Neilson, *Chem. Mater.*, 2019, **31**, 7248–7254.
- [18] A. J. Martinolich, J. A. Kurzman and J. R. Neilson, *J. Am. Chem. Soc.*, 2016, **138**, 11031–11037.
- [19] A. J. Martinolich and J. R. Neilson, *Chem. Mater.*, 2017, **29**, 479–489.
- [20] R. D. Shannon, D. B. Rogers, and C. T. Prewitt, *Inorg. Chem.*, 1971, **10**, 713–718.
- [21] P. K. Todd and J. R. Neilson, *J. Am. Chem. Soc.*, 2019, **141**, 1191–1195.
- [22] P. K. Todd, A. M. M. Smith, and J. R. Neilson, *Inorg. Chem.*, 2019, **58**, 15166–15174.

- [23] O. Menge, *Z. Anorg. Chem.*, 1911, **72**, 162–218.
- [24] E. Jänecke, *Z. Anorg. Chem.*, 1950, **261**, 213–225.
- [25] A. Jain, S. P. Ong, G. Hautier, W. Chen, W. D. Richards, S. Dacek, S. Cholia, D. Gunter, D. Skinner, G. Ceder, and K. A. Persson, *APL Mater.*, 2013, **1**, 011002.
- [26] C. J. Bartel, A. W. Weimer, S. Lany, C. B. Musgrave, and A. M. Holder, *npj Comput. Mater.*, 2019, **5**(1), 4.
- [27] G. Hautier, S. P. Ong, A. Jain, C. J. Moore, and G. Ceder, *Phys. Rev. B: Condens. Matter Mater. Phys.*, 2012, **85**(15), 155208.
- [28] C. J. Bartel, S. L. Millican, A. M. Deml, J. R. Rumpitz, W. Tumas, A. W. Weimer, S. Lany, V. Stevanovic, C. B. Musgrave, and A. M. Holder, *Nat. Commun.*, 2018, **9**, 4168.
- [29] D. R. Lide, *CRC Handbook of Chemistry and Physics, 84th Edition*, CRC Press, 2003.
- [30] L. Ratke and P. W. Voorhees, *Growth and Coarsening: Ostwald Ripening in Materials Processing*, Springer-Verlag, 2002.
- [31] A. Anedda, E. Fortin, F. Ledda, and A. Serpi, *Phys. Status Solidi B*, 1982, **114**, K143–K146.
- [32] K. Maeda, R. Abe, and K. Domen, *J. Phys. Chem. C*, 2011, **115**, 3057–3064.
- [33] S. H. Elder, L. H. Doerr, F. J. Disalvo, J. B. Parise, D. Guyomard, and J. M. Tarascon, *Chem. Mater.*, 1992, **4**, 928–937.
- [34] A. Miura, K. Tadanaga, E. Magome, C. Moriyoshi, Y. Kuroiwa, T. Takahiro, and N. Kumada, *J. Solid State Chem.*, 2015, **229**, 272–277.
- [35] H. Kageyama, K. Hayashi, K. Maeda, J. P. Attfield, Z. Hiroi, J. M. Rondinelli, and K. R. Poeppelmeier, *Nat. Commun.*, 2018, **9**, 772.
- [36] X. Jia, A. Lynch, Y. Huang, M. Danielson, I. Lang’at, A. Milder, A. E. Ruby, H. Wang, S. A. Friedler, A. J. Norquist, and J. Schrier, *Nature*, 2019, **573**, 251–255.

## Chapter 3 Novel polymorphs of $\text{Li}_3\text{YCl}_6$

### 3-1 $\text{Li}^+$ -ion conducting ternary halide electrolytes

$\text{Li}^+$ -ion conducting electrolytes are the key materials for all-solid-state batteries, which are attractive next-generation batteries with high safety and high energy density. Various oxides, sulfides, halides, and hydride solid electrolytes have been developed<sup>[1-3]</sup>. Halide-based electrolytes have been studied for several decades; however, except for the high-temperature phase of  $\text{Li}_3\text{InBr}_6$ , their conductivities had been considered to be rather small at room temperature<sup>[4]</sup>. After the discovery of the high  $\text{Li}^+$  conductivity of  $\text{Li}_3\text{YCl}_6$  and  $\text{Li}_3\text{YBr}_6$ , *i.e.*,  $10^{-4}$ – $10^{-3}$   $\text{S cm}^{-1}$  at room temperature, and their capability as solid electrolytes for all-solid-state batteries reported by Asano *et al.*<sup>[5]</sup>, many ternary halides have been (re)investigated as solid electrolytes<sup>[6-13]</sup>, some of which have shown a conductivity of  $10^{-4}$ – $10^{-3}$   $\text{S cm}^{-1}$ . The highly conductive features of  $\text{Li}^+$  in chlorides, bromides, and iodides can be understood as large and monovalent halide ions with weak interactions with  $\text{Li}^+$ , which facilitates fast  $\text{Li}^+$  diffusion. Moreover, their wide electrochemical stability window and good stability toward oxide cathodes are advantageous<sup>[8]</sup>.

Ternary chlorides are formally represented as  $\text{Li}_3\text{MX}_6$  ( $\text{M}$  = rare earth metal of La-Lu, Sc, Y;  $\text{X}$  = Cl, Br) composed of closely packed structures of  $\text{X}^-$  and different cation occupancies in octahedral holes<sup>[8]</sup>. For instance,  $\text{Li}_3\text{YCl}_6$  is composed of hexagonal close-packed  $\text{Cl}^-$ , whereas  $\text{Li}_3\text{YBr}_6$  is composed of cubic close-packed  $\text{Br}^-$ <sup>[5]</sup>. Cation arrangements depend on the composition and synthesis method<sup>[5, 11, 12]</sup>. For  $\text{Li}_3\text{YCl}_6$ , ball milling and subsequent heating produced low crystallinity and crystallized samples. Furthermore, cooling after heat treatment resulted in structural diversity, which was further explained by the formation of stacking faults and local structural changes. Considering that different cation arrangements of  $\text{Li}_3\text{ErCl}_6$  show comparable calculated energies<sup>[11]</sup>, the cation arrangements of these halides would be rather flexible. Indeed, various average structures as well as local structures have been reported, even for the same composition, which depends on the synthesis methods and

heating temperatures<sup>[11, 14, 15]</sup>. The effect of the Li<sup>+</sup> concentration<sup>[9]</sup>, the blocking effect of rare earth elements<sup>[9, 11]</sup>, the disordering of M atoms<sup>[11]</sup>, and the volume and distortion of MCl<sub>6</sub><sup>3- [11, 16]</sup> on Li<sup>+</sup> conductivities have been discussed. Because these cation sublattices are correlated with ion conductivities, the polymorphs with different cation arrangements can exhibit higher conductivity than that of the reported one.

### **3-2 Aim of this chapter**

The synthesis of Li<sub>3</sub>YCl<sub>6</sub> was examined using in-situ XRD to demonstrate the low-temperature synthesis based on the assumption that the weak Coulombic attraction between the anion, Cl<sup>-</sup>, and cation, Li<sup>+</sup>, in the starting materials leads to high diffusion rates and lowers the reaction temperature. Herein, a new metastable phase of Li<sub>3</sub>YCl<sub>6</sub> with a smaller lattice and high Li<sup>+</sup> conductivity was discovered through in situ X-ray diffraction (XRD) analysis of the solid-state reaction between LiCl and YCl<sub>3</sub>. Structural analysis using XRD and neutron diffraction, X-ray absorption, and <sup>7</sup>Li NMR revealed different arrangements of Li and Y in the crystal structure.

## **3-3 Experimental Section**

### **3-3-1 Experimental**

All experiments were conducted within a glovebox filled with Ar at a dew point of  $\approx -80$  °C. LiCl (Kojundo Chemical Lab.) was used as a reagent after grinding with a planetary ball mill (Fritsch P-7) while YCl<sub>3</sub> (Sigma-Aldrich) was used as received without any treatment. The mortars were dried overnight at 50 °C under a vacuum. In addition, LiCl and YCl<sub>3</sub> were mixed and sealed in a quartz glass capillary under a vacuum. Synchrotron X-ray diffraction patterns were measured at the BL02B2 beam line of Spring-8 (Proposal Nos. 2019B1195). The wavelength of the incident X-rays was 0.496391 Å. The sample capillaries were heated at a rate of 30 K min<sup>-1</sup>. Diffraction data were collected using a

high-resolution one-dimensional semiconductor detector<sup>[17]</sup>. The X-ray diffraction data were analyzed using the Rietveld method with the RIETAN-FP program<sup>[18]</sup>, and crystal structures were drawn using the VESTA program<sup>[19]</sup>. An S-Li<sub>3</sub>YCl<sub>6</sub> powder sample was synthesized by heating a cold-pressed pellet of 3LiCl+YCl<sub>3</sub> at 595 K for over 50 h. The time-of-flight powder neutron diffraction data of S-Li<sub>3</sub>YCl<sub>6</sub> were collected on the SPICA diffractometer installed at the Material and Life Science Facility in the Japan Proton Accelerator Research Complex (Proposal No. 2017L1302). The neutron diffraction pattern obtained with the low-angle bank and backscattering bank was refined using the Z-Rietveld program<sup>[20]</sup>. In this paper, the result for the backscattering bank was shown in the main body since the resolution with the backscattering bank is higher than that of the low-angle bank. XANES measurements of the Y *K* edge were performed at the Aichi Synchrotron Radiation Center BL5S1 (Proposal number: 2022D3006). The local structures around Y were refined from the EXAFS spectra using the ATHENA and ARTEMIS software packages<sup>[21]</sup>. Solid-state NMR spectra of <sup>7</sup>Li were recorded on a 500 MHz Bruker NMR spectrometer with a magic angle spinning at 15 kHz.

The ionic conductivity of pelletized S-Li<sub>3</sub>YCl<sub>6</sub> was determined using electrochemical impedance spectroscopy. The sample powder was pressed into a pellet with a diameter of 6 mm, and two stainless steel current collectors were used. Electrochemical impedance spectroscopy (ESI) was measured in an Ar-filled glovebox under  $\approx 280$  MPa using an impedance analyzer (SI1260) within the frequency range of 0.1–107 Hz at a voltage amplitude of 30 mV. During the ESI measurement, the dew point of the Ar-filled glovebox was below  $-70$  °C. Scanning electron microscopy (SEM) and transmission electron microscopy (TEM) observations were performed by JEM-2010 and JIB-4600F, respectively, without exposure to air during sample transfer.

### 3-3-2 Rietveld Refinement Details

The crystal structure, proposed in Figure 3-6, was proposed in three steps. First, Rietveld refinement of SXRD was conducted by optimizing the lattice parameters, occupancies, and displacement parameters of Y (2*b*) and Cl (6*f*). First, the occupancy and the displacement parameter of Cl (6*f*) were fixed, and those of Y (2*b*) were refined. Second, those of both Y (2*b*) and Cl (6*f*) were refined. As these occupancies converged at 0.5 and 1 within the error, I applied further refinements with these fixed occupancies. Final refinement was performed with fixed atomic occupancy and displacement parameters determined by ND. I applied an ND diffraction to refine those of Li (4*d*). There are two ND settings. One is a low-angle bank showing a wide-angle range, but the resolution is moderate. The other is a backscattering bank giving only a low-angle range, but the resolution is high. Accordingly, the reported crystal structure shown in Table 3-1 is about the ND measurement at the backscattering bank while the diffraction data of the low-angle bank shows no diffraction peaks corresponding to the superlattice of the proposed lattice. For the ND refinements, the first refinement was performed with the isotropic atomic displacement parameter of Li(4*d*), and further refinements were performed with anisotropic atomic displacement parameters for Li ( $U_{11}(\text{Li})$  and  $U_{33}(\text{Li})$ ). Although the anisotropic displacement parameters for Y and Cl had been refined, these atomic displacement parameters were isotropic within error. Thus, Y and Cl were refined using isotropic displacement parameters. Furthermore, each refinement of occupancies of Li(4*d*), Y (2*b*), and Cl (6*f*) did not converge with better refinement parameters.

### 3-4 Results

In-situ XRD upon heating the mixture of LiCl and YCl<sub>3</sub> at 30 K min<sup>-1</sup>, as shown in Figure 3-1a, shows that the diffraction peak at  $\approx 5.0^\circ$  appeared above 450 K and an additional peak appeared at  $\approx 5.4^\circ$  above 600 K. Both peaks can be assigned to the reported hexagonal Li<sub>3</sub>YCl<sub>6</sub><sup>[5]</sup>, however, the

absence of the peak at  $\approx 5.4^\circ$  in the temperature range of 450–600 K indicates the formation of a new phase with higher symmetry and/or smaller lattice parameters. Hereafter, the previously reported phase and this new phase are referred to as T- $\text{Li}_3\text{YCl}_6$  and S- $\text{Li}_3\text{YCl}_6$ , respectively. The new phase, S- $\text{Li}_3\text{YCl}_6$ , can be assigned as the cell with a  $1/\sqrt{3}$  a-axis and a similar c-axis to the reported T- $\text{Li}_3\text{YCl}_6$ . Thus, the reaction can be formulated as follows, and their mass fraction using the structural model described later is shown in Figure 3-1b. Refinement profiles with different temperatures were shown in figure 3-2.

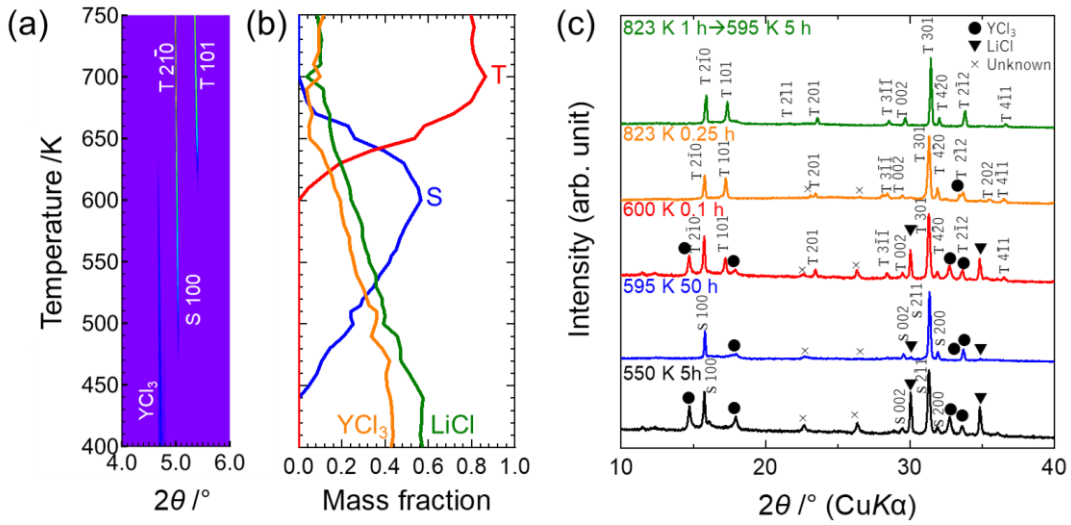
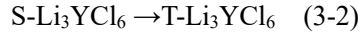
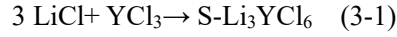


Figure 3-1: Solid-state reaction between  $\text{LiCl}$  and  $\text{YCl}_3$  for the synthesis of  $\text{Li}_3\text{YCl}_6$ : a) temperature dependence of synchrotron X-ray diffraction and b) mass fraction calculated from Rietveld refinement results. The wavelength of incident X-ray was 0.496391 Å. c) XRD patterns of  $\text{Li}_3\text{YCl}_6$  synthesized at different temperatures and heating times measured using  $\text{CuK}\alpha$  radiation ( $\lambda = 1.5418$  Å).



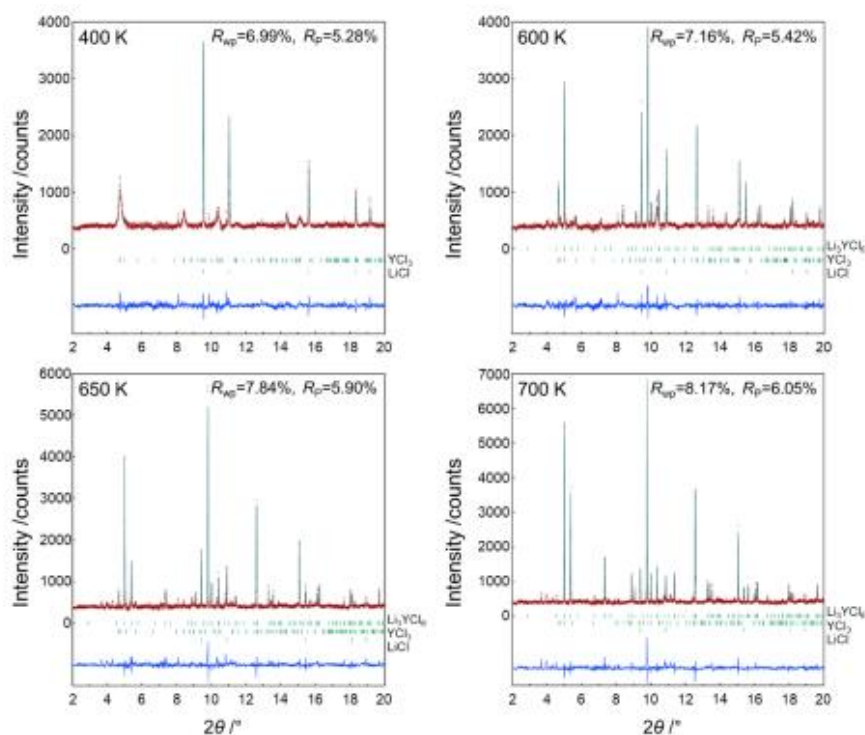


Figure 3-2: Rietveld profiles of in situ XRD patterns for LiCl and YCl<sub>3</sub> measured at 400, 600, 650, and 700 K. The experimental and calculated results are indicated by red dots and green solid lines, respectively, in each graph. The bottom blue lines are the residuals.

The S-Li<sub>3</sub>YCl<sub>6</sub> sample synthesized by heating a mixture of LiCl and YCl<sub>3</sub> at 595 K for 50 h produced a nearly single-phase powder (Figure 3-1c), which was used for structural and impedance measurements, as described later. There were two unindexed peaks. No electron diffraction spots corresponding to these unindexed peaks were seen in the electron diffraction image (Figure 3-3), indicating no superlattice structures of S-Li<sub>3</sub>YCl<sub>6</sub>. Intensities of these unindexed peaks increased when the sample was exposed to air for  $\approx 1$  min before heating (Figure 3-4). Although these diffractions cannot be assigned as oxides, chlorides, and oxychlorides recorded in the ICSD database, these peaks are likely attributed to an unknown impurity phase composed of Li<sup>+</sup>, Y<sup>3+</sup>, O<sup>2-</sup>, OH<sup>-</sup>, CO<sub>3</sub><sup>2-</sup>, Cl<sup>-</sup>, or H<sub>2</sub>O. After the report of the synthesis of S-Li<sub>3</sub>YCl<sub>6</sub>, E. sebt *et al.* found that these broad peaks can be

observed for the sample synthesized by milling and heat treatment. The details of the structural differences are discussed in the next chapter. A decrease in temperature remained in the unreacted starting materials, whereas a further increase in temperature above 600 K yielded a T-Li<sub>3</sub>YCl<sub>6</sub> phase even after heating for only 15 min. At 595 K, the heat duration from 5 to 500 h showed S-Li<sub>3</sub>YCl<sub>6</sub> and did not bring about significant changes (Figure 3-5). Furthermore, the synthesis by heating to 823 K and then annealing at 595 K for 50 h did not yield the S-Li<sub>3</sub>YCl<sub>6</sub>; thus, the phase transition from S-Li<sub>3</sub>YCl<sub>6</sub> to T-Li<sub>3</sub>YCl<sub>6</sub> was irreversible, and S-Li<sub>3</sub>YCl<sub>6</sub> was metastable. As reported, the ball milling of LiCl and YCl<sub>3</sub> together and subsequent heating did not produce S-Li<sub>3</sub>YCl<sub>6</sub><sup>[5, 6]</sup>. YCl<sub>3</sub> is composed of a hexagonal close-packed anion arrangement as that of Li<sub>3</sub>YCl<sub>6</sub> but only one-third octahedral site is filled with Y. Thus, I considered that a topotactic reaction occurs by diffusing Li and Cl from LiCl into YCl<sub>3</sub> even below 600 K, leading to the formation of metastable S-Li<sub>3</sub>YCl<sub>6</sub> that cannot be obtained through high-temperature heating or ball milling treatment.

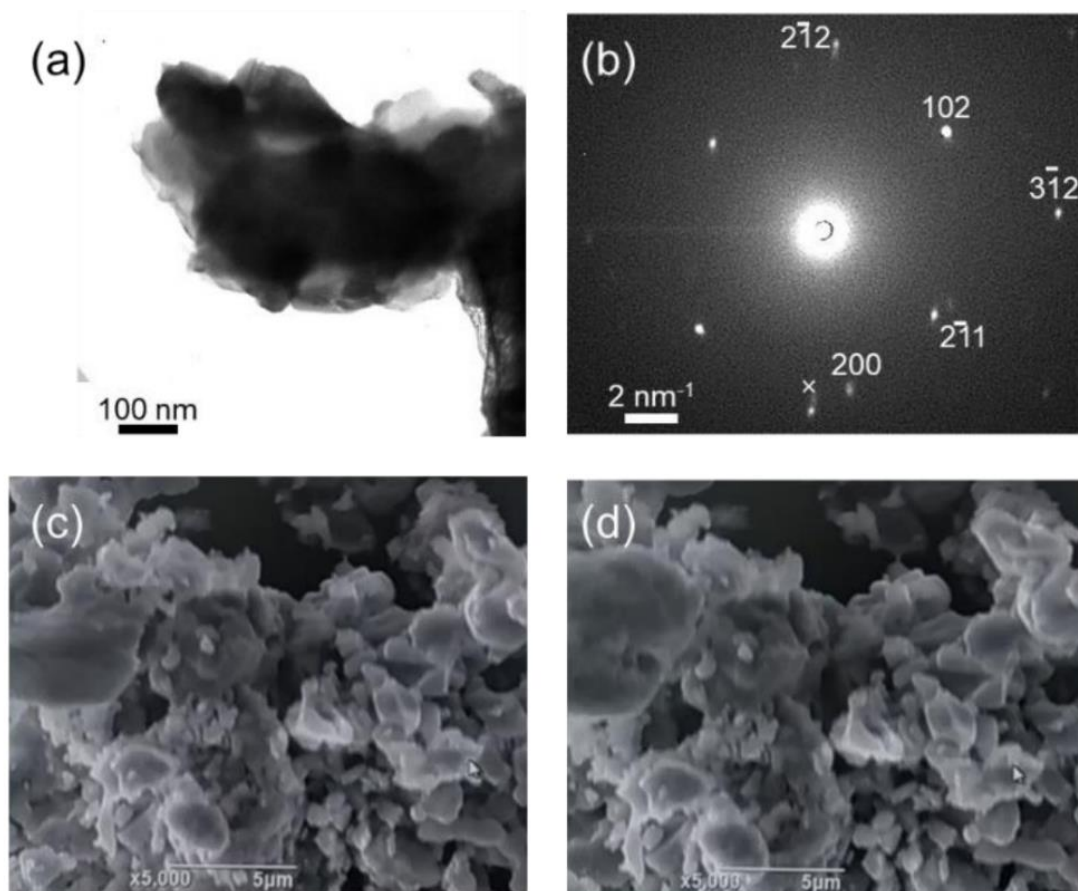


Figure 3-3: Electron microscope image of  $\text{S-Li}_3\text{YCl}_6$ . (a) TEM and (b) corresponding electron diffraction images of  $\text{S-Li}_3\text{YCl}_6$  synthesized by heating at 595 K for 50 h. The numbers are indexes of  $\text{S-Li}_3\text{YCl}_6$ , and a weak spot shown as X cannot be indexed as  $\text{S-Li}_3\text{YCl}_6$ . SEM images of the sample (c) after  $\sim 10$  sec and (d) after  $\sim 60$  sec. The change in morphology indicates an unstable feature under the electron beam

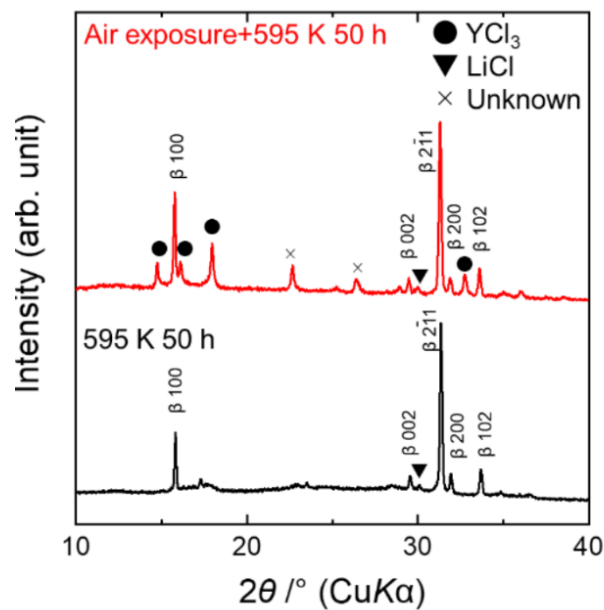


Figure 3-4: in-situ XRD patterns of  $\text{Li}_3\text{YCl}_6$  synthesized at 595 K with/without exposure to Air. Precursor powders were pressed into a pellet with a diameter of 6mm and exposed to air for  $\sim 1$  minute before being sealed in an evacuated quartz tube.

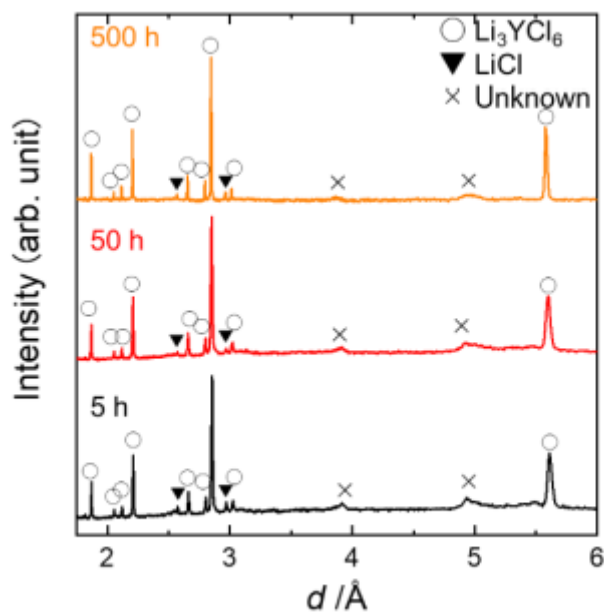


Figure 3-5: Time dependence of ex-situ XRD patterns of  $\text{Li}_3\text{YCl}_6$  heated at 595 K for 5 to 500 h. The  $d$  value was set as an x-axis to compare patterns obtained by synchrotron XRD and conventional XRD.

Figure 3-6a–c shows the Rietveld profiles of S-Li<sub>3</sub>YCl<sub>6</sub> obtained through SXRD and ND, respectively. The main peaks in SXRD are assigned to the hexagonal cell with lattice parameters of  $a = 6.4604(1)$  Å and  $c = 6.0302(1)$  Å. Both the  $a$ - and  $c$ -axes are expanded (per the same number of atoms) when compared with the lattice parameters of T-Li<sub>3</sub>YCl<sub>6</sub> synthesized at 700 K ( $1/\sqrt{3}a = 6.45754(2)$  Å,  $c = 6.02606(9)$  Å [Table 3-1]). Thus, the density of S-Li<sub>3</sub>YCl<sub>6</sub> is lower than that of T-Li<sub>3</sub>YCl<sub>6</sub>. Rietveld refinement results of neutron diffraction data collected at the backscattering bank are shown in Table 3-2; the refinement results of SXRD and ND collected at low angle bank are summarized in Table 3-3 and 3-4, respectively. S-Li<sub>3</sub>YCl<sub>6</sub> was crystallized with the space group  $P\bar{3}c1$ . Here, Cl<sup>−</sup> is in a hexagonal close-packed anion arrangement, and every cation is octahedrally coordinated. There are two cation sites, as shown in Figure 3-6d. One is the Wyckoff position  $2b$ , where Y is statistically occupied at the edge of the lattice along the  $c$ -axis. In comparison with T-Li<sub>3</sub>YCl<sub>6</sub>, S-Li<sub>3</sub>YCl<sub>6</sub> would be less stable because more Y<sup>3+</sup> statistically exists as the second nearest atoms induce the electronic repulsion between Y<sup>3+</sup>: Pauling's third rule. The phase transition from S- to T-Li<sub>3</sub>YCl<sub>6</sub> can be understood by the migration of Y along the  $c$ -axis, as shown in red arrows in Figure 3-6d. The other is the Wyckoff position  $4d$ , where the Li occupation is 0.75. The off-stoichiometric and antisite defects did not improve the Rietveld fitting. The bond length between Li ( $4d$ ) and Cl ( $2.62871(4)$  Å) was longer than that in LiCl ( $2.5730(15)$  Å; ICSD No. 52235), leading to the bond valence sum slightly less than one (0.857). The atomic displacement parameter of Y site was smallest ( $U = 0.0133(2)$  Å<sup>2</sup>), larger in Cl ( $U = 0.02097(6)$  Å<sup>2</sup>), and the largest in Li ( $U = 0.0522(4)$  Å<sup>2</sup>), as expected. Larger atomic displacement parameter of Li<sup>+</sup> along the  $c$ -axis was proposed:  $U_{11} = U_{22} = 0.03710(6)$  Å<sup>2</sup>,  $U_{33} = 0.0858(13)$  Å<sup>2</sup>. This anisotropic displacement suggests the Li<sup>+</sup> conduction path along the  $c$ -axis; this is also supported by the bond valence sum map (Figure 3-7). Compared with T- and S-Li<sub>3</sub>YCl<sub>6</sub> phases, no significant difference in effective coordination numbers<sup>[22]</sup> derived by average structure is determined by diffraction techniques.

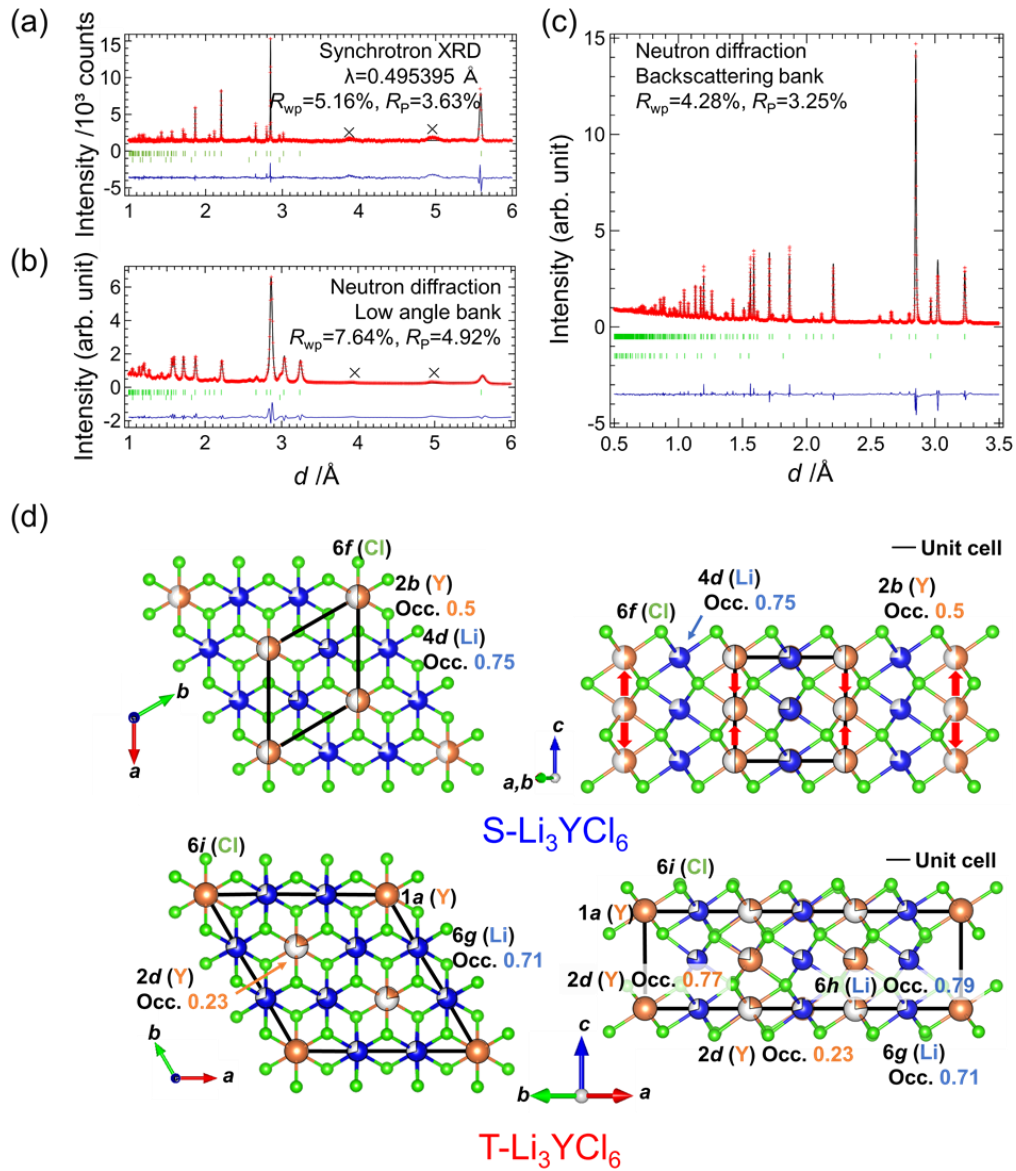


Figure 3-6: Rietveld profiles of a) XRD and b,c) neutron diffraction data for  $S\text{-Li}_3\text{YCl}_6$  synthesized at 595 K. The measurements are conducted at room temperature. Cross marks denote unidentified small diffraction peaks likely from an unknown impurity phase. The experimental and calculated results are indicated by dots and solid lines, respectively. The green bars are the diffraction position of  $S\text{-Li}_3\text{YCl}_6$  and  $\text{LiCl}$ . The bottom lines are the residuals. d) Crystal structure of  $S\text{-Li}_3\text{YCl}_6$  and  $T\text{-Li}_3\text{YCl}_6$ . The unit cells are denoted through the black lines, and the migrations of Y during the phase transition from  $T\text{-Li}_3\text{YCl}_6$  to  $S\text{-Li}_3\text{YCl}_6$  are represented by red arrows.

Table 3-1: Synthesis condition, lattice parameters, and ionic conductivity of  $\text{Li}_3\text{YCl}_6$ .

	Precursor, molar ratio	Heating condition	Lattice parameter /Å		Ionic conductivity at 25 °C /S·cm <sup>-1</sup>
			<i>a</i>	<i>c</i>	
S- $\text{Li}_3\text{YCl}_6$ (this paper)	LiCl: $\text{YCl}_3$ =3:1	595 K for 50 h	6.4604(1)	6.0302(1)	$1.2 \times 10^{-4}$
T- $\text{Li}_3\text{YCl}_6$ (this paper)	LiCl: $\text{YCl}_3$ =3:1	700 K for 0.5 h	11.1848(1)	6.02606(9)	$1.4 \times 10^{-5}$
Ball-milled $\text{Li}_3\text{YCl}_6$ (1)	LiCl: $\text{YCl}_3$ =3:1	Only ball milling	11.2217(7)	6.05517(6)	$5.1 \times 10^{-4}$
T- $\text{Li}_3\text{YCl}_6$ (2)	LiCl: $\text{YCl}_3$ =3:1	Annealing at 823 K	11.1969(0)	6.03112(3)	$\sim 3.0 \times 10^{-5}$
T- $\text{Li}_3\text{YCl}_6$ (3)	LiCl: $\text{YCl}_3$ =3:1.1	823 K for 1 week + slow cooling	11.20934(9)	6.04694(9)	$\sim 6.1 \times 10^{-5}$
T- $\text{Li}_3\text{YCl}_6$ (4)	LiCl: $\text{YCl}_3$ =3:1.1	823 K for 5 min + air quenching	11.20926(9)	6.0382(1)	$\sim 3.7 \times 10^{-5}$

Table 3-2: Fractional coordinates, occupancies, atomic displacement parameters, and bond valence sum of S-Li<sub>3</sub>YCl<sub>6</sub>. Neutron diffraction was collected at the backscattering bank. Anisotropic atomic displacement parameters,  $U_{11}$  and  $U_{33}$ , were used for Li. Lattice parameter:  $a = 6.464667(7)$  Å,  $c = 6.043934(14)$  Å,  $R_{wp} = 4.28\%$ ,  $R_p = 3.25\%$ ,  $R_e = 1.15\%$ ,  $R_B(\text{Li}_3\text{YCl}_6) = 8.53\%$ ,  $R_F(\text{Li}_3\text{YCl}_6) = 10.25\%$ , Space group:  $165 P\bar{3}c1$ , The second phase: 2.5 mass% of LiCl

Atom	Wyckoff position	Occupancy	Atomic coordinates			$U/\text{\AA}^2$	$BVS$
			$a$	$b$	$c$		
Y	$2b$	0.5	0	0	0	0.0113(2)	3.206
Li	$4d$	0.75	1/3	2/3	0	0.0533(4)*	0.853
Cl	$6f$	1	1/3	0	1/4	0.02097(6)	0.961

\*  $U_{11}(\text{Li}) = U_{22}(\text{Li}) = 0.03710(6)$  Å<sup>2</sup>,  $U_{33}(\text{Li}) = 0.0858(13)$  Å<sup>2</sup>.

Table S3-3: Fractional coordinates, occupancies, atomic displacement parameters, and bond valence sum of  $\beta$ -Li<sub>3</sub>YCl<sub>6</sub> refined using synchrotron X-ray diffraction. Anisotropic atomic displacement parameters for Li were fixed, and the isotropic displacement of Y and Cl were refined. Lattice parameters:  $a = 6.4604(1)$  Å,  $c = 6.0302(1)$  Å,  $R_{wp} = 5.16\%$ ,  $R_p = 3.63\%$ ,  $R_R = 50.34\%$ ,  $R_e = 2.58\%$ ,  $S = 2.0009$ , Space group:  $165 P\bar{3}c1$ , The second phase: 9.32 mass% of LiCl

Atom	Wyckoff position	Occupancy	Atomic coordinates			$U/\text{\AA}^2$	$BVS$
			$a$	$b$	$c$		
Y	$2b$	0.5	0	0	0	0.008(1)	3.234
Li	$4d$	0.75	1/3	2/3	0	0.013(fix)	0.86
Cl	$6f$	1	1/3	0	1/4	0.017(1)	0.969



Table S3-4: Fractional coordinates, occupancies, and atomic displacement parameters of  $\beta$ -Li<sub>3</sub>YCl<sub>6</sub> refined using Neutron diffraction collected at low angle bank. Isotropic atomic displacement parameters for Y and Cl were fixed, and anisotropic atomic displacement parameters,  $U_{11}$  and  $U_{33}$ , were employed only for Li. Lattice parameter:  $a = 6.47636(2)\text{\AA}$ ,  $c = 6.05680(4)\text{\AA}$ ,  $R_{wp} = 9.51\%$ ,  $R_p = 5.51\%$ ,  $R_e = 0.45\%$ ,  $R_B(\text{Li}_3\text{YCl}_6) = 10.18\%$ ,  $R_F(\text{Li}_3\text{YCl}_6) = 3.72\%$ , Space group:  $165 P\bar{3}c1$ , The second phase: 2.6 mass% of LiCl

Atom	Wyckoff position	Occupancy	Atomic coordinates			$U/\text{\AA}^2$	BVS
			$a$	$b$	$c$		
Y	$2b$	0.5	0	0	0	0.0110(3)	3.163
Li	$4d$	0.75	1/3	2/3	0	0.0649(7)*	0.841
Cl	$6f$	1	1/3	0	1/4	0.0206(1)	0.948

\*  $U_{11}(\text{Li}) = U_{22}(\text{Li}) = 0.058(1)\text{\AA}^2$ ,  $U_{33}(\text{Li}) = 0.079(1)\text{\AA}^2$ .

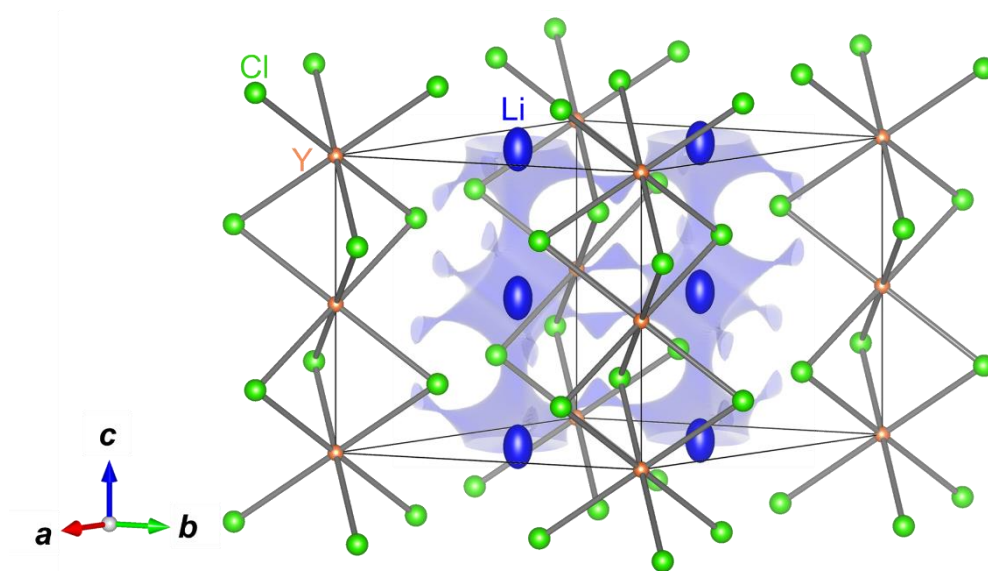


Figure 3-7: Oak ridge thermal ellipsoid plot drawing (75% thermal ellipsoids) and bond valence sum (BVS) mapping for Li<sub>3</sub>YCl<sub>6</sub>. Blue, orange, and green ellipsoids represent lithium, yttrium, and chlorine, respectively. The isosurface is drawn in transparent blue at a BVS mismatch level of 0.35 valence units for Li<sup>+</sup>.

To understand the local structure, the EXAFS of Y and the NMR spectra of  $\text{Li}^{7}$  were measured. The Y  $K$ -edge X-ray absorption spectra of S- and T- $\text{Li}_3\text{YCl}_6$  were shown in Figure 3-8. The XANES and EXAFS spectra of S- and T- $\text{Li}_3\text{YCl}_6$  were comparable (Fig. 3-8a and b). The Fourier-transformed EXAFS data of S- $\text{Li}_3\text{YCl}_6$  fit well with the simulated data based on the model without the nearest-neighbor Y-Y, as depicted in the inset of Figure 3-8c. Accordingly, the structural model composed of 1D atomic chains with alternate Y was proposed (Figure 3-8d). The difference between S- and T- $\text{Li}_3\text{YCl}_6$  reflects in the periodicity of the different lattices. In the T-phase, Y is located at the lattice corner, whereas in the S-phase, Y loses this periodicity. This periodicity appears as the 101 diffraction peak in the XRD pattern, as described above.

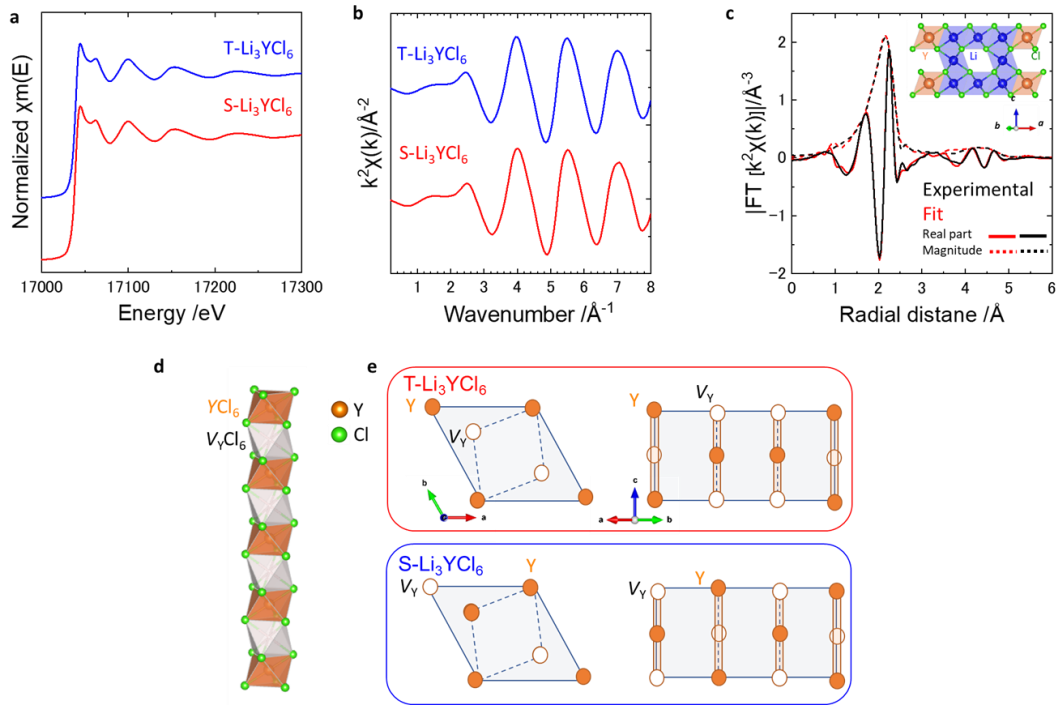


Figure 3-8: Local structure of Y in  $\text{Li}_3\text{YCl}_6$ . (a) XANES spectra (b) EXAFS spectra of  $\text{Li}_3\text{YCl}_6$  (c) Fourier transform of EXAFS analysis of T- $\text{Li}_3\text{YCl}_6$ ; inset shows the structure model for XANES derived from XRD. (d) Schematic image of the  $\text{YCl}_6$ - $V_Y\text{Cl}_6$ - $\text{YCl}_6$  chain along the  $c$ -axis.  $V_Y$  denotes the vacancy at the Y site. (e) Schematic image of the arrangement of chains in S- and T- $\text{Li}_3\text{YCl}_6$ .

The  $^7\text{Li}$  NMR spectra of the  $\text{Li}_3\text{YCl}_6$  polymorphs exhibited peaks at different positions. Figure 3-9 shows NMR spectra with different scales. Peaks of  $^7\text{Li}$  were observed at  $-0.80$  ppm for S- $\text{Li}_3\text{YCl}_6$  and  $-0.89$  ppm for T- $\text{Li}_3\text{YCl}_6$ . The negative shift in the peak maximum indicates a lower electronic density around Li. The peak was the sharpest for T- $\text{Li}_3\text{YCl}_6$ , and a slightly broader peak was observed for S- $\text{Li}_3\text{YCl}_6$ . The different widths of these peaks suggest that the number of sites in which Li can exist is greater in S- $\text{Li}_3\text{YCl}_6$  than in T- $\text{Li}_3\text{YCl}_6$ .

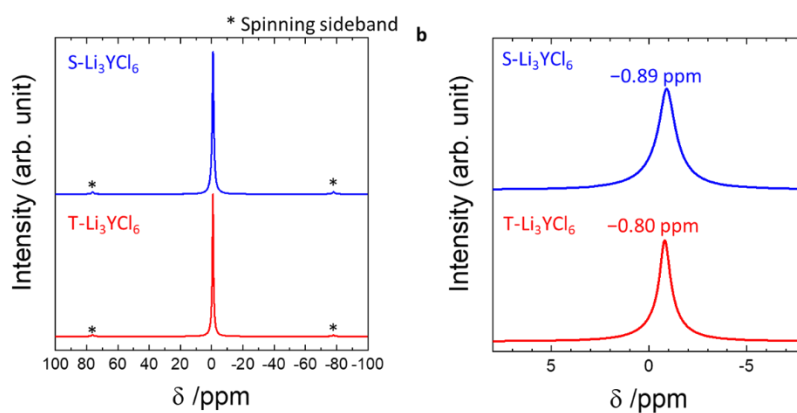


Figure 3-9: NMR spectra of S- and T-  $\text{Li}_3\text{YCl}_6$  were collected with the magic angle spinning of 15 kHz.

Figure 3-10 shows the electrochemical impedance spectroscopy and temperature dependence of  $\text{Li}^+$  conductivity acquired through impedance measurements of cold-pressed pellets of T- and S- $\text{Li}_3\text{YCl}_6$  synthesized at 595 and 700 K, respectively.  $\text{Li}^+$  conductivity for S- $\text{Li}_3\text{YCl}_6$  ( $1.2 \times 10^{-4} \text{ S cm}^{-1}$ ) at near room temperature is higher than that in the T- $\text{Li}_3\text{YCl}_6$  ( $1.4 \times 10^{-5} \text{ S cm}^{-1}$ ), and their activation energies of S- $\text{Li}_3\text{YCl}_6$  ( $11 \text{ kJ mol}^{-1}$ ) are lower than that in the T- $\text{Li}_3\text{YCl}_6$  ( $16 \text{ kJ mol}^{-1}$ ). The values of the pre-exponential factor of the Arrhenius equation, which are a product of the carrier concentrations and diffusion coefficients (equation [3-6]), are comparable. The ionic conductivity  $\sigma$  can be expressed as a product of the number of ions per unit volume,  $N$ , ionic charge,  $q$ , and mobility of the particles.

$$\mu:\sigma = Nq\mu \quad (3-3)$$

From the Nernst-Einstein equation,  $\mu$  can be also given by:

$$\mu = Dq/k_B T \quad (3-4)$$

The influence of temperature on the diffusion constant  $D$  is represented by the Arrhenius equation.

$$D = D_0 \cdot \exp(-E_a/RT) \quad (3-5)$$

From eq. (3-3), (3-4), and (3-5),  $\sigma$  is given by:

$$\ln \sigma = -E_a/R(1/T) + \ln (Nq^2 D_0/k_B T) \quad (3-6)$$

Although I cannot deny the possibility that these conductivities are limited by the grain boundaries, the crystallographic feature of the S-Li<sub>3</sub>YCl<sub>6</sub> can account for the high Li<sup>+</sup> conductivity and low activation energy. The larger lattice parameters (per atom) due to the repulsion between Y<sup>3+</sup> widens the Li<sup>+</sup> pathway in S-Li<sub>3</sub>YCl<sub>6</sub>, and thus lowers the activation energy and increases the conductivity of S-Li<sub>3</sub>YCl<sub>6</sub>.

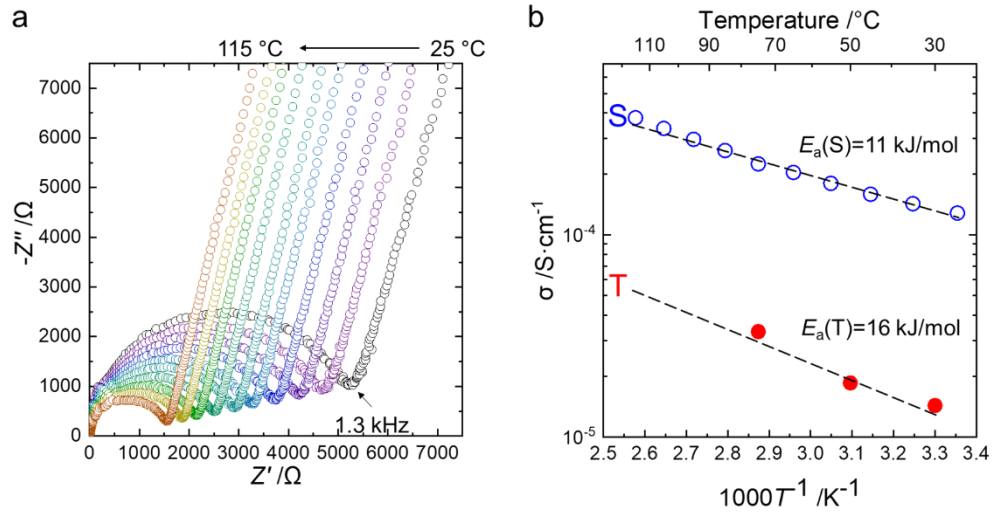


Figure 3-10: a) Nyquist plots of the AC impedance measurements of S-Li<sub>3</sub>YCl<sub>6</sub>. b) Temperature dependence of Li<sup>+</sup> conductivity in T- and S-Li<sub>3</sub>YCl<sub>6</sub> synthesized at 700 and 595 K, respectively. The values of the pre-exponential factor in the Arrhenius equation were calculated as 4.31 for S-Li<sub>3</sub>YCl<sub>6</sub> synthesized at 595 K and 4.68 for T-Li<sub>3</sub>YCl<sub>6</sub> synthesized at 700 K.

### 3-5 Summary

Notably, the a-axis lattice parameter of S-Li<sub>3</sub>YCl<sub>6</sub> is  $1/\sqrt{3}$ , which is the first example of a Li<sub>3</sub>MCl<sub>6</sub> system. The low density of S-Li<sub>3</sub>YCl<sub>6</sub> due to large electronic repulsion between Y<sup>3+</sup> can account for the low activation energy of Li<sup>+</sup> transport and high conductivity. Comparison with the ionic conductivity of other reported T-Li<sub>3</sub>YCl<sub>6</sub> samples (Table S1, Supporting Information) shows that the conductivity of S-Li<sub>3</sub>YCl<sub>6</sub> was higher than that of reported T-Li<sub>3</sub>YCl<sub>6</sub>, but was lower than that of Li<sub>3</sub>YCl<sub>6</sub> synthesized by ball-milling. The diffraction pattern of the ball-milled Li<sub>3</sub>YCl<sub>6</sub> can be indexed as T-Li<sub>3</sub>YCl<sub>6</sub>, but the broad diffraction peak does not yield a detailed structural model<sup>[5]</sup>. Nonetheless, the partial disordering of Y is discussed because a broad and weak 101 diffraction peak was detected, which only appeared in the case of T-Li<sub>3</sub>YCl<sub>6</sub>. A related study on the effect of Er disorder in ball-milled Li<sub>3</sub>ErCl<sub>6</sub> proposed that this disorder broadens the diffusion channel of Li<sup>[11]</sup>; we can understand the enhancement of Li<sup>+</sup> conduction in S-Li<sub>3</sub>YCl<sub>6</sub> with the disordered Y site in a similar way. However, the best cation arrangement for achieving high Li conductivity is still unclear. In this work, a new cation arrangement in Li<sub>3</sub>YCl<sub>6</sub> with a different unit cell was discovered through the solid-state reaction between LiCl and YCl<sub>3</sub> powders, the conductivity of which is higher than that of T-Li<sub>3</sub>YCl<sub>6</sub> (Table S1, Supporting Information). Thus, in situ analyses of solid-state reactions can facilitate the detection of various cation orderings, which would aid in the discovery of new ion conductors with high conductivity.

### 3-6 References

- [1] M. Shoji, E. J. Cheng, T. Kimura, and K. Kanamura, *J. Phys. D: Appl. Phys.*, 2019, **52**, 103001.
- [2] F. Zheng, M. Kotobuki, S. Song, M. O. Lai, and L. Lu, *J. Power Sources*, 2018, **389**, 198.
- [3] A. Manthiram and X. Yu, S. Wang, *Nat. Rev. Mater.*, 2017, **2**, 16103.
- [4] Y. Tomita, A. Fuji-i, H. Ohki, K. Yamada, and T. Okuda, *Chem. Lett.*, 1998, **27**, 223.
- [5] T. Asano, A. Sakai, S. Ouchi, M. Sakaida, A. Miyazaki, and S. Hasegawa, *Adv. Mater.*, 2018, **30**, 1803075.
- [6] X. Li, J. Liang, N. Chen, J. Luo, K. R. Adair, C. Wang, M. N. Banis, T. K. Sham, L. Zhang, S. Zhao, S. Lu, H. Huang, R. Li, and X. Sun, *Angew. Chem., Int. Ed. Engl.*, 2019, **58**, 16427.
- [7] R. Schlem, A. Banik, S. Ohno, E. Suard, and W. G. Zeier, *Chem. Mater.*, 2021, **33**, 327.
- [8] X. Li, J. Liang, X. Yang, K. R. Adair, C. Wang, F. Zhao, and X. Sun, *Energy Environ. Sci.*, 2020, **13**, [1429.
- [9] J. Liang, X. Li, S. Wang, K. R. Adair, W. Li, Y. Zhao, C. Wang, Y. Hu, L. Zhang, S. Zhao, S. Lu, H. Huang, R. Li, Y. Mo, and X. Sun, *J. Am. Chem. Soc.*, 2020, **142**, 7012.
- [10] K.-H. Park, K. Kaup, A. Assoud, Q. Zhang, X. Wu, and L. F. Nazar, *ACS Energy Lett.*, 2020, **5**, 533.
- [11] R. Schlem, S. Muy, N. Prinz, A. Banik, Y. Shao-Horn, M. Zobel, and W. G. Zeier, *Adv. Energy Mater.*, 2019, **10**, 1903719.
- [12] C. Yu, Y. Li, K. R. Adair, W. Li, K. Goubitz, Y. Zhao, M. J. Willans, M. A. Thijs, C. Wang, F. Zhao, Q. Sun, S. Deng, J. Liang, X. Li, R. Li, T.-K. Sham, H. Huang, S. Lu, S. Zhao, L. Zhang, L. van Eijck, Y. Huang, and X. Sun, *Nano Energy*, 2020, **77**, 105097.
- [13] S. Akihiro, A. Tetsuya, S. Masashi, N. Yusuke, M. Akinobu, and H. Shinya, US16/911447, 2020.
- [14] H. Kwak, D. Han, J. Lyoo, J. Park, S. H. Jung, Y. Han, G. Kwon, H. Kim, S. T. Hong, K. W. Nam, and Y. S. Jung, *Adv. Energy Mater.*, 2021, **11**, 2003190.

- [15] L. Zhou, C. Y. Kwok, A. Shyamsunder, Q. Zhang, X. Wu, and L. F. Nazar, *Energy Environ. Sci.*, 2020, **13**, 2056.
- [16] R. Schlem, A. Banik, S. Ohno, E. Suard, and W. G. Zeier, *Chem. Mater.*, 2021, **33**, 327.
- [17] S. Kawaguchi, M. Takemoto, K. Osaka, E. Nishibori, C. Moriyoshi, Y. Kubota, Y. Kuroiwa, and K. Sugimoto, *Rev. Sci. Instrum.*, 2017, **88**, 085111.
- [18] F. Izumi and K. Momma, *Solid State Phenom.*, 2007, **130**, 15.
- [19] K. Momma and F. Izumi, *J. Appl. Crystallogr.*, 2008, **41**, 653.
- [20] R. Oishi, M. Yonemura, Y. Nishimaki, S. Torii, A. Hoshikawa, T. Ishigaki, T. Morishima, K. Mori, and T. Kamiyama, *Nucl. Instrum. Methods Phys. Res., Sect. A*, 2009, **600**, 94.
- [21] B. Ravel and M. Newville, *J. Synchrotron Radiat.*, 2005, **12**, 537–541.
- [22] R. Hoppe, *Z. Kristallogr. - Cryst. Mater.*, 1979, **150**, 23.

## Chapter 4 The thermodynamic stability of $\text{S-Li}_3\text{YCl}_6$

### 4-1 Introduction

#### 4-1-1 Definition of the metastability

The term metastable is defined in the oxford languages as follows; theoretically unstable but so long-lived as to be stable for practical purposes. That is, the stable product must be settled to describe the other polymorph as metastable, and the metastable products are just trapped at the local minima of the energy landscape for a certain period. Figure 4-1 shows an image of the energy landscape of blocks with different stacking patterns. The structure on the right is metastable within the area inside the green line but becomes the stable phase in the area shown by the blue square. In addition, the state in the middle of the collapse on the right can also be regarded as a metastable phase that exists momentarily. Furthermore, the relation of the stability between starting materials and product polymorphs can be changed depending on the situation since the free energy is affected by the temperature, pressure, and surface area<sup>[1]</sup>.

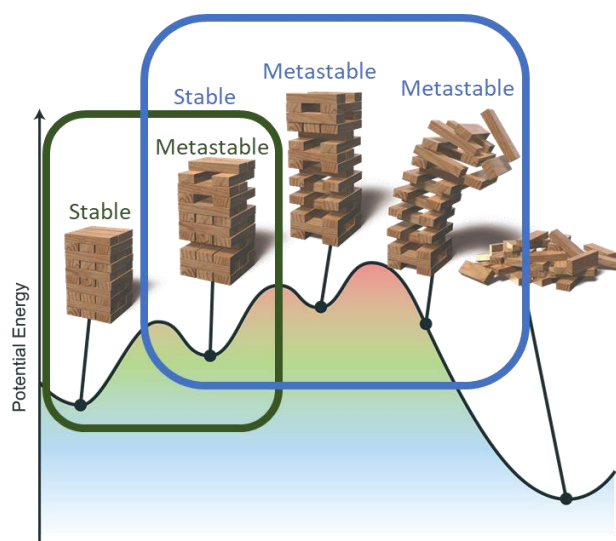


Figure 4-1 Schematic image of energy landscape where structures locate energy minima, and the ground state is a completely disordered structure.



#### 4-1-2 Variety of observed and hypothetical structures with metastability

Metastability affords a variability of crystal structures, resulting in different properties than that of a stable phase<sup>[2-11]</sup>. One of the most popular metastable materials is glass. The glass including simple  $\text{SiO}_2$  is less thermodynamically stable than crystals at ambient temperature. Metastable ion conductors such as  $\text{Li}_3\text{PS}_4$ <sup>[8]</sup> and  $\text{LiAlCl}_4$ <sup>[12]</sup> formed via solid-state synthesis also have been studied as a candidate for solid electrolytes. Figure 4-2 shows the formation enthalpy of reported and hypothetical structures calculated based on the density functional theory (DFT)<sup>[1]</sup>. Some polymorphs showed higher energies than the ground state, suggesting that the free energy calculated based on the DFT does not rationalize the synthesizability as mentioned in the literature.

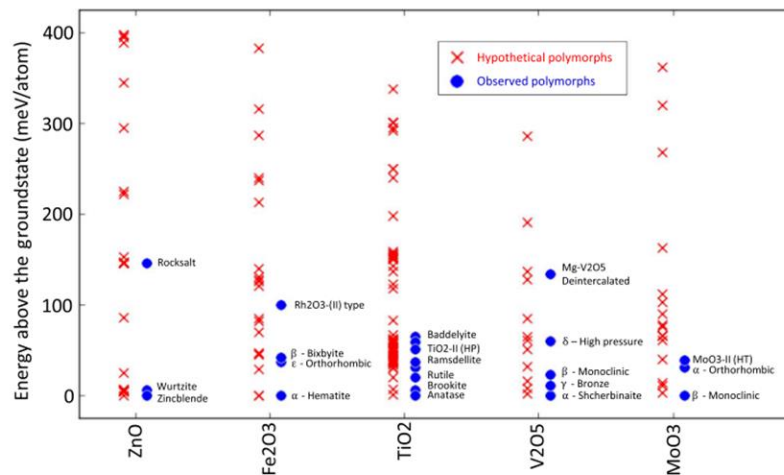


Figure 4-2: Examples of the formation enthalpy calculated based on the DFT. The reported structure does not always exhibit the minimum formation enthalpies.

#### 4-1-3 Examples of metastable materials obtained by different synthesis ways

Metastable materials have been synthesized using different processes. The melt quenching technique is the most common technique for the production of glass materials ranging from traditional silica to metallic glass<sup>[13-16]</sup>. Also, ball-milling and subsequent heat treatment are now widely employed to

synthesize glass electrolytes<sup>[17]</sup>. With some retention of liquid structure, glass possesses a more random structure than stable crystalline. Another synthesis way for metastable materials is the use of well-designed starting material and low-temperature heating to interrupt and prevent the formation of a stable product. For example, physical vapor deposition controls the layered structure of layered Pb-Nb selenides. Further heat treatment can selectively synthesize six different polymorphs with different stacking patterns of PbSe<sub>2</sub> and NbSe<sub>2</sub> layers<sup>[18-20]</sup>.

#### 4-1-4 Kinetical representation of synthesis strategies

Figure 4-3 shows the reaction coordinate diagrams corresponding to the type of kinetical stabilization methods by A. Martinolich and J. Neilson<sup>[21]</sup>. They introduce the reaction coordinate diagrams to understand and design the reaction only using kinetics. In Fig. 4-3a, the reaction spontaneously proceeds without any control. Therefore, the synthesis reaction has been modified to stabilize the materials with metastability under ambient conditions. Fig 4-3b depicts the reaction coordinate diagram of kinetic trapping. Product 1, which is stable only under specific pressure and temperature conditions kinetically trapped by the rapid change of the conditions. Another way to obtain a thermodynamically metastable product is kinetic control (fig. 4-3(c)). The activation energies of reactions are controlled, and the metastable product 2 can be synthesized. The *Chimie douce* approaches including sol-gel methods and topochemical reactions have been employed as kinetic control techniques to synthesize the metastable oxide materials<sup>[22]</sup>. The use of redox reaction, flux, and structure-controlled raw materials alter the activation energies. However, the term kinetic control does not represent the change in the relation of free energy between products.

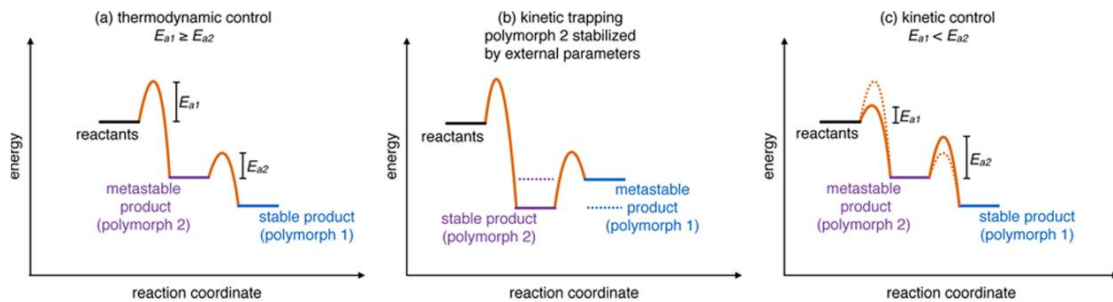


Figure 4-3. Reaction coordinate diagrams depicting (a) thermodynamic control, (b) kinetic trapping, and (c) kinetic control by A. Martinolich and J. Neilson in Ref. 21.

#### 4-1-5 Thermodynamic representation of metastability

The energy diagram which describes the change in the relative stabilities between polymorphs is already proposed by W. Sun *et al.* and the metastability of polymorph 2 in fig. 4-3b is named as the remnant metastability<sup>[1]</sup>. The energy diagram visualizes the free energies as the function of the multiple thermodynamic parameters including temperature and pressure. In this paper, the absolute temperature is chosen as the x-axis of the free energy diagram to simplify the discussion in the following sections. In fig. 4-3, the main feature of remnant metastable materials is that the free energy curve of the metastable material intersects with that of the stable product at a certain temperature. As a result, polymorph 1 become remnant metastable while polymorph 2 is stable at ambient temperature. The energy curves for remnant metastability are shown in Fig. 4-4. Remnant metastable polymorph can be synthesized by once stabilizing at high temperature and quenching to room temperature. An example of remnant metastable materials is glass as shown in section 4-3.

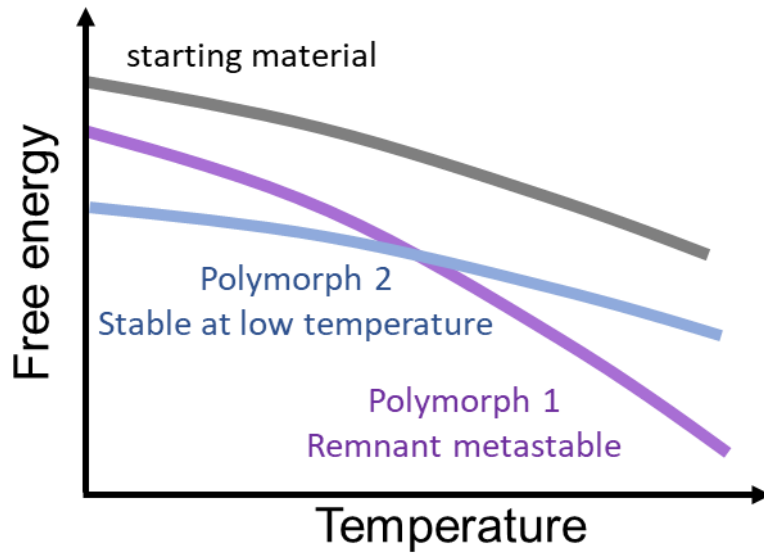


Figure 4-4: Free energy curves representing the remnant metastability.

#### 4-1-6 Evaluation of the energy curve

The temperature dependence of the free energy of materials has been evaluated by thermal analysis. Although differential scanning calorimetry, DSC, has been employed to observe heat effects associated with phase transitions. The monitoring of the small change in the enthalpy of polymorphs with a similar structure and calculation of the enthalpy and entropy of materials from experiments are difficult for heat-flux DSC. A high heating rate is required to obtain well-defined peaks and separate them from the background.

In recent years, with the development of computers such as DFT and machine learning, the enthalpy of the formation of matter has become widely available. The enthalpy change ( $\Delta H$ ) can be obtained by integrating the specific heat capacity,  $C_p$ , measured by DSC with temperature (Eqn. (4-1)). Furthermore, entropy can also be calculated from the integration of  $C_p$  from initial temperature,  $T_i$ , to final temperature,  $T_f$ , expressed by the following equation (4-2) while the entropy at 0 K must be estimated assuming the Debye extrapolation.

$$\Delta H = \int_{T_i}^{T_f} C_p dT \quad (4-1)$$

$$S(T_f) = S(T_i) + \int_{T_i}^{T_f} \frac{C_p dT}{T} \quad (4-2)$$

#### 4-1-7 Remnant and intermediate metastability

In this paper, two different types of metastabilities are (re)categorized as a remnant and intermediate metastability. The types of metastability where metastable material located between the intermediate of starting materials and stable material in the free energy diagram were referred to as intermediate metastability. Figure 4-5 depicts the energy diagram of intermediate metastability. The major difference from the remnant metastable system is that the free energy curve of the metastable material does not cross that of a stable product. Therefore, metastable materials cannot be obtained by heat treatment of stable polymorph, and kinetic control and low-temperature synthesis are required to suppress the phase transition from metastable to a stable product. Examples of intermediate metastable materials can be layered chalcogenides such as VS<sub>2</sub><sup>[23, 24]</sup> and CuSe<sub>2</sub><sup>[25]</sup>, and Pb-Nb selenides<sup>[18-20]</sup>.

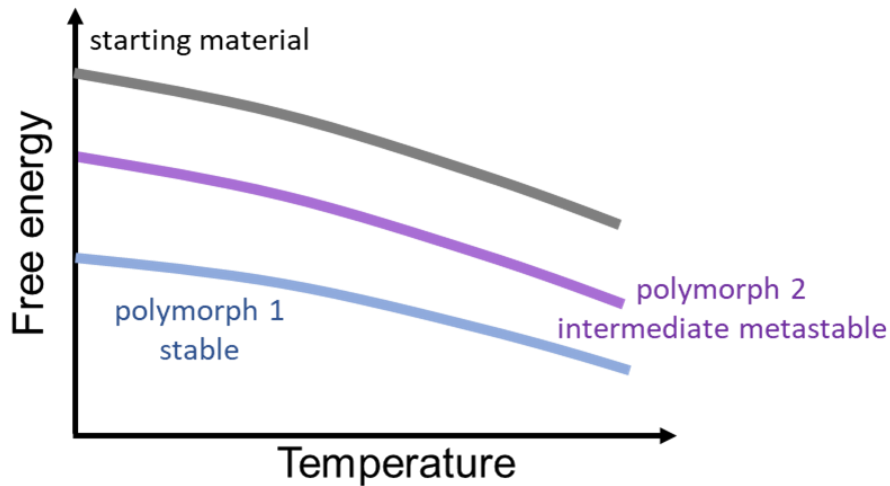


Figure 4-5: Energy diagram representing the intermediate metastability.

Since the temperature dependence of products is different in the remnant and intermediate testability, the reversibility of the phase transition from metastable to the stable product can be used to determine the type of metastability. The phase transition is reversible in the remnant metastable system whereas the transition is irreversible for the intermediate one at a moderate temperature. This classification is possible for materials with similar specific heat capacities, which are difficult to measure by DSC measurement. Moreover, the type of metastability can be useful for understanding and designing the synthesis process of metastable materials. By clarifying metastability, we can understand whether a substance is metastable without depending on temperature, or it becomes stable at a certain temperature, and we can predict the synthesis process including starting materials, heating temperature, and cooling speed.

#### **4-1-8 Aim of this chapter**

In Chapter 3, a novel polymorph S-Li<sub>3</sub>YCl<sub>6</sub> was synthesized. The lower density of S-Li<sub>3</sub>YCl<sub>6</sub> can explain the lower activation energy of Li<sup>+</sup> conduction and higher Li<sup>+</sup> conductivity than that of reported T-Li<sub>3</sub>YCl<sub>6</sub>. On the other hand, an understanding of stability between polymorphs is insufficient. To determine the type of metastability of Li<sub>3</sub>YCl<sub>6</sub>, annealing of T-Li<sub>3</sub>YCl<sub>6</sub> is performed, and the reversibility of phase transitions was examined. Furthermore, the presence of defects and compositional changes in Li<sub>3</sub>YCl<sub>6</sub> were discussed to rationalize the stability of S-Li<sub>3</sub>YCl<sub>6</sub> at low temperatures.

#### **4-2 Experimental section**

The synthesis and annealing of T-Li<sub>3</sub>YCl<sub>6</sub> were performed under the Ar atmosphere with a dew point of -80 °C. T-Li<sub>3</sub>YCl<sub>6</sub> was synthesized by heating the mixture of 3LiCl+YCl<sub>3</sub> at 700 K for 3 h and fast cooling by taking the crucible out from the furnace soon after the end of heating. The annealing temperature was determined to be 573 K since the phase transition occurred at 595 K in the in-situ

measurement. The samples were annealed for 6 h and cooled to 300 K in the furnace. The XRD patterns of the samples before and after annealing were collected by the Rigaku mini flex with CuK $\alpha$  radiation.

#### 4-3 Result: Reversibility of phase transition revealed by XRD measurements

Figure 4-6 shows the XRD patterns of T-Li<sub>3</sub>YCl<sub>6</sub> before and after the annealing. Before the annealing, the main peaks were indexed as T-Li<sub>3</sub>YCl<sub>6</sub>. The annealing brought about significant change in the relative intensities of peaks such as 101 and 2 $\bar{1}$ 0. Although the additional peaks around emerged, the main products were indexed as S-Li<sub>3</sub>YCl<sub>6</sub>. These results indicated that the phase transition of Li<sub>3</sub>YCl<sub>6</sub> was reversible. Additionally, the peaks of LiCl emerged after annealing, and the peaks of 17 and 24 ° after annealing suggested the existence of impurity phases.

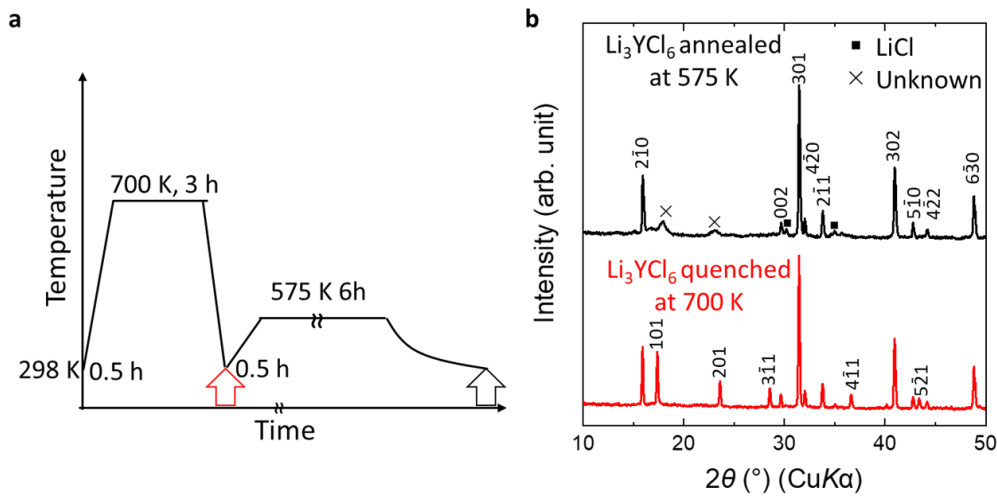


Figure 4-6: Temperature profile of heating and XRD patterns of T-Li<sub>3</sub>YCl<sub>6</sub> before and after annealing at 573 K. Decrease in the intensity of the 101 peaks of T-phases upon annealing indicated the formation of the S-phases.

#### 4-4 Discussion

The changes in XRD patterns before and after annealing indicate that T-Li<sub>3</sub>YCl<sub>6</sub> was metastable at 573 K against the S phase. Fig. 4-7 shows a schematic diagram of the energy diagram of the Li<sub>3</sub>YCl<sub>6</sub> crystal polymorph in which the S phase has remnant metastability. The free energy of T-Li<sub>3</sub>YCl<sub>6</sub> is lower at higher temperatures than that of the S phase, as the phase transition from S to T phase was observed by in-situ XRD, and becomes higher near room temperature as suggested by annealing. Also, the temperature at which the S-phase and T-phase energy curves cross each other was estimated to be around 573-595 K since the phase transition occurred above 600 K and was reversible at 573 K. The Black arrow indicates the change of free energy during the annealing.

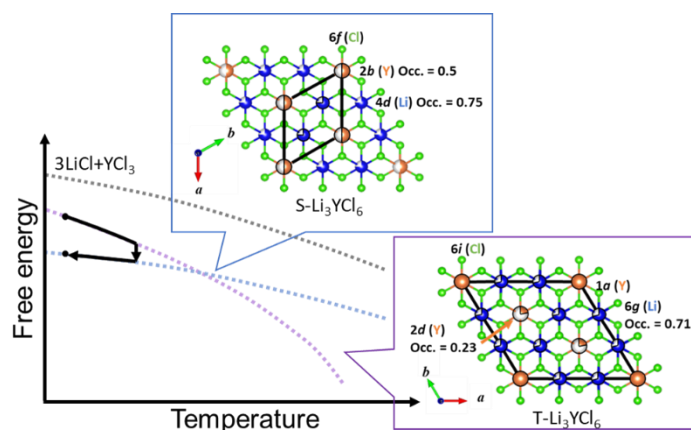


Figure 4-7: Schematic image of energy diagram for Li<sub>3</sub>YCl<sub>6</sub> polymorphs.

Although the experimental results suggest the remnant metastability of T-Li<sub>3</sub>YCl<sub>6</sub>, the origin remnant metastability of T-phases was not fully rationalized from the structural point of view. As shown in chapter 3, T-phases possessed slightly smaller volumes per formula unit, and Y in the structure exhibit the ordering which resulted in a larger lattice than S-phases. I believe that the formation of stacking faults and the formation of LiCl with the decomposition of Li<sub>3</sub>YCl<sub>6</sub> may have resulted in the lowering of the free energy of the S-phase at low temperatures, promoting the phase transition from the T-phase to the S-phase.



After the report of S-Li<sub>3</sub>YCl<sub>6</sub>, E.sebti *et al.* reported that Li<sub>3</sub>YCl<sub>6</sub> synthesized by ball milling and heat treatment of 3LiCl and YCl<sub>3</sub> possess stacking faults of layers along the c-axis<sup>[26]</sup>. Fig. 4-8(a-c) shows the structure model including stacking faults and the Rietveld profile of Li<sub>3</sub>YCl<sub>6</sub> obtained by ball milling. The structure consists of four layers as shown. Furthermore, heating at 500 K suppressed the defects, and around 10% of stacking faults remained (fig. 4-8(d)). Refinement using a stacking fault model reproduces the XRD pattern containing broad peaks with 2θ near 2.7 and 3.6° at an incident X-ray wavelength of 0.24177 Å, which correspond to 17.5 and 23.6° for Cu Kα radiation.

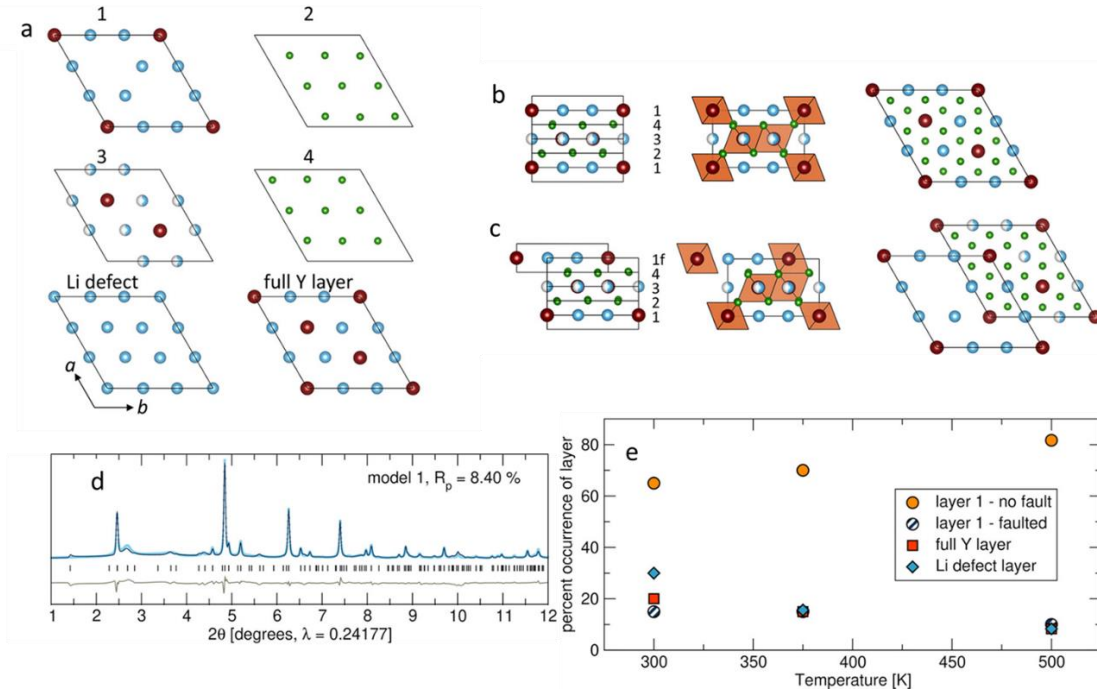


Figure 4-8: (a) Image of layers contained in the stacking model (b,c) crystal structure models without and with stacking faults (d) Rietveld profile refined with stacking faults model (e) percentage of occurrence of stacking faults for samples with different heat treatment temperatures by E. Sebti *et al.*

These results suggest that a large number of defects were contained in the structure of the products obtained by annealing. Similar to the mechanochemically synthesized samples<sup>[26]</sup>, two peaks were observed around 17° and 24° after annealing. Furthermore, LiCl was produced during annealing and additional peaks appeared at 30° and 35°, as shown in Fig. 4-6. Long-term periodic three-dimensional

structures containing so many defects as detected by XRD are thermodynamically unstable. On the other hand, many two-dimensional layered compounds with structural defects have been synthesized. For example, the thermoelectric material  $\text{In}_2\text{Ge}_2\text{Te}_6$ <sup>[27]</sup> and the catalyst  $\text{Bi}_{12}\text{O}_{17}\text{Cl}_2$ <sup>[28]</sup> crystallize in the structures containing stacking faults, corrugations, and dislocations. Therefore, the presence of stacking faults in  $\text{Li}_3\text{YCl}_6$  suggests the two-dimensional nature of the structure. The annealing results also demonstrate the compositional flexibility of the Li-Y-Cl compounds. In the phase diagram<sup>[29]</sup>,  $\text{Li}_3\text{YCl}_6$  is a linear compound, although the use of excess  $\text{YCl}_3$  leads to a nearly single-phase product. These reports suggest the presence of hexagonal  $\text{Li}_{3-x}\text{YCl}_{6-x}$  in addition to the reported orthorhombic phase<sup>[30]</sup>.

Future experiments on compositional and entropy changes are required to understand the reaction quantitatively.

#### 4-5 Conclusion

In chapter 4, I introduced the types of metastability; remnant and intermediate metastability from the thermodynamical point of view, and the free energy curves of intermediate metastability were depicted. The difference in the temperature dependence of products was emphasized by separating remnant and intermediate metastability. Furthermore, it became possible to theoretically understand which of the previously proposed kinetic controls and kinetic trapping are required to generate metastable phases since the categorization of the type of metastability is independent of the synthesis procedures. Moreover, the stability of  $\text{Li}_3\text{YCl}_6$  polymorphs was determined by annealing the quenched sample. From the annealing of  $\text{Li}_3\text{YCl}_6$ , it was clarified that the phase transition was reversible, and the high-temperature phase of  $\text{Li}_3\text{YCl}_6$  which is referred to as T- $\text{Li}_3\text{YCl}_6$  is “remnant metastable” at low temperatures below 573 K. Furthermore, it was suggested that the annealing produced S- $\text{Li}_3\text{YCl}_6$  containing many defects in the crystal structure.

#### 4-6 References

- [1] W. Sun, S. T. Dacek, S. P. Ong, G. Hautier, A. Jain, W. D. Richards, A. C. Gamst, K. A. Persson, and G. Ceder, *Sci. Adv.* 2016, **2**(11), e1600225.
- [2] A. W. Sleight, *Phys. Today*, 1991, **44**(6), 24–30.
- [3] H. Oike, M. Kamitani, Y. Tokura, and F. Kagawa, *Sci. Adv.*, 2018, **4**(10), 1–7.
- [4] X. Tan, S. Geng, Y. Ji, Q. Shao, T. Zhu, P. Wang, Y. Li, and X. Huang, *Adv. Mater.*, 2020, **32**(40), 1–7.
- [5] A. K. Cheetham, *Science*, 1994, **264**(5160), 794–795.
- [6] Y. Yao, Z. Huang, P. Xie, S. D. Lacey, R. J. Jacob, H. Xie, F. Chen, A. Nie, T. Pu, M. Rehwoldt, D. Yu, M. R. Zachariah, C. Wang, R. Shahbazian-Yassar, J. Li, and L. Hu, *Science*, 2018, **359**(6383), 1489–1494.
- [7] M. Tatsumisago, Y. Shinkuma, and T. Minami, *Nature*, 1991, **354**(6350), 217–218.
- [8] K. Kaup, L. Zhou, A. Huq, and L. F. Nazar, *J. Mater. Chem. A*, 2020, **8**(25), 12446–12456.
- [9] K. Kanazawa, S. Yubuchi, C. Hotehama, M. Otoyama, S. Shimono, H. Ishibashi, Y. Kubota, A. Sakuda, A. Hayashi, and M. Tatsumisago, *Inorg. Chem.*, 2018, **57**(16), 9925–9930.
- [10] K. Karube, J. S. White, N. Reynolds, J. L. Gavilano, H. Oike, A. Kikkawa, F. Kagawa, Y. Tokunaga, H. M. Rønnow, Y. Tokura, and Y. Taguchi, *Nat. Mater.*, 2016, **15**(12), 1237–1242.
- [11] F. Kagawa and H. Oike, *Adv. Mater.*, 2017, **29**(25), 1601979.
- [12] N. Tanibata, S. Takimoto, K. Nakano, H. Takeda, M. Nakayama, and H. Sumi, *ACS Mater. Lett.*, 2020, **2**(8), 880–886.
- [13] J. E. Shelby and M. Lopes, Introduction to Glass Science and Technology. *The Royal Society of Chemistry*, 2005.
- [14] W. Klement, R. H. Willens, and P. O. L. Duwez, *Nature*, 1960, **187**, 869–870.
- [15] P. Duwez, *J. Vac. Sci. Technol. B*, 1983, **1**, 218–221.

- [16] H. W. Sheng, W. K. Luo, F. M. Alamgir, J. M. Bai, and E. Ma, *Nature*, 2006, **439**, 419–425.
- [17] T. Rojac and M. Kosec, High-Energy Ball Milling, 6 - Mechanochemical Synthesis of Complex Ceramic Oxides; Sopicka-Lizer, M. B. T.-H.-E. B. M., Ed.; *Woodhead Publishing*, 2010, 113–148.
- [18] M. Esters, M. B. Alemayehu, Z. Jones, N. T. Nguyen, M. D. Anderson, C. Grosse, S. F. Fischer, and D. C. Johnson, *Angew. Chemie - Int. Ed.*, 2015, **54**, 1130–1134.
- [19] K. Ariyoshi, K. Yuzawa, and Y. Yamada, *J. Phys. Chem. C*, 2020, **124**, 8170–8177.
- [20] J. Bai, W. Sun, J. Zhao, D. Wang, P. Xiao, J. Y. P. Ko, A. Huq, G. Ceder, and F. Wang, *Chem. Mater.*, 2020, **32**(23), 9906–9913.
- [21] A. J. Martinolich and J. R. Neilson, *Chem. Mater.*, 2017, **29**(2), 479–489.
- [22] J. Gopalakrishnan, *Chem. Mater.*, 1995, **7**(7), 1265–1275.
- [23] D. W. Murphy, C. Cros, F. J. Di Salvo, and J. V. Waszczak, *Inorg. Chem.*, 1977, **16**, 3027–3031.
- [24] P. Poddar and A. K. Rastogi, *J. Phys. Condens. Matter*, 2002, **14**, 2677–2689.
- [25] A. J. Martinolich, R. F. Higgins, M. P. Shores, and J. R. Neilson, *Chem. Mater.*, 2016, **28**, 1854–1860.
- [26] E. Sebt, H. A. Evans, H. Chen, P. M. Richardson, K. M. White, R. Giovine, K. P. Koirala, Y. Xu, E. Gonzalez-Correa, C. Wang, C. M. Brown, A. K. Cheetham, P. Canepa, and R. J. Clément, *J. Am. Chem. Soc.*, 2022, **144**(13), 5795–5811.
- [27] R. Lefèvre, D. Berthebaud, O. Lebedev, O. Pérez, C. Castro, S. Gascoin, D. Chateigner, and F. Gascoin, *J. Mater. Chem. A*, 2017, **5** (36), 19406–19415.
- [28] D. Kato, O. Tomita, R. Nelson, M. A. Kirsanova, R. Dronskowski, H. Suzuki, C. Zhong, C. Tassel, K. Ishida, Y. Matsuzaki, C. M. Brown, K. Fujita, K. Fujii, M. Yashima, Y. Kobayashi, A. Saeki, I. Oikawa, H. Takamura, R. Abe, H. Kageyama, T. E. Gorelik, and A. M. Abakumov, *Adv. Funct. Mater.*, 2022, **32** (41), 2204112.
- [29] Y. Sun, G. Bian, W. Tao, C. Zhai, M. Zhong, and Z. Qiao, *Calphad*, 2012, **39**, 1–10.

[30] J. Liang, E. Maas, J. Luo, X. Li, N. Chen, K. R. Adair, W. Li, J. Li, Y. Hu, J. Liu, L. Zhang, S. Zhao, S. Lu, J. Wang, H. Huang, W. Zhao, S. Parnell, R. I. Smith, S. Ganapathy, M. Wagemaker, and X. Sun, *Adv. Energy Mater.*, 2022, **12** (21), 2103921.

## Chapter5 General conclusion

In summary, I have demonstrated the selective synthesis of novel polymorphs of  $\text{MgCr}_2\text{S}_4$  and discovered a new polymorph of  $\text{Li}_3\text{YCl}_6$ , and discussed the type of metastability using the  $\text{Li}_3\text{YCl}_6$  polymorph as an example.

The fine particle of  $\text{MgCr}_2\text{S}_4$  was obtained by low-temperature synthesis involving the use of fluxes and metathesis reactions, as shown in Chapter 2. The thermodynamic driving force of the reaction was enhanced by the metathesis reaction, and sufficient diffusion was achieved using molten salt flux. These results indicate that the inclusion of thermodynamically stable by-products and liquid phases can be an attractive method for the synthetic design of new functional materials. Although the understanding of complex reactions using parameters such as diffusion coefficient and standard enthalpy of formation is not straightforward, recent advances in DFT and machine learning have enabled the calculation of thermodynamic values for many hypothetical structures. It will become possible to theoretically design reactions that selectively synthesize target substances at low temperatures by combining the knowledge of reaction processes and thermodynamic parameters obtained by in-situ measurements of model compounds and the computational calculation, respectively.

Chapter 3 showed the low-temperature synthesis of a new polymorph of  $\text{Li}_3\text{YCl}_6$ . The in-situ XRD measurements of the reaction between  $\text{LiCl}$  and  $\text{YCl}_3$  revealed the existence of a novel polymorph at middle temperature, and its crystal structure and Li conducting properties were examined. Furthermore, the combination of XRD, ND, XAS, and NMR revealed slightly different average and local structures of polymorphs. These results indicated that in-situ measurement is a powerful tool to explore new materials and emphasize the importance of heating conditions to precisely control the structure to tune its properties. The discovery of a new polymorph of  $\text{Li}_3\text{YCl}_6$  demonstrated that the vast compositional space available for mechanochemical synthesis is worth exploring using advanced in-situ techniques

and low-temperature solid-state reactions.

In Chapter 4, I proposed intermediate metastability in addition to remnant metastability to understand metastability from a thermodynamic perspective. Intermediate metastable is a concept that corresponds to the stability in which a stable phase is irreversibly generated as the reaction progresses, such as decomposition. Therefore, a metastable phase cannot be obtained from a stable phase by heat treatment. On the other hand, the relative stability between two products depends on thermodynamic handles, and it is possible to reversibly interconvert the product phases upon quenching or annealing in remnant metastability. From the annealing of the known phase of  $\text{Li}_3\text{YCl}_6$ , a reversible phase transition from the new phase to the reported phase was observed. This suggests that the known phase is remnant metastable at low temperatures and is a high-temperature phase.

Overall, selective synthesis of thermodynamically competing phases was achieved by low-temperature reactions. Furthermore, the reclassification of metastability allowed us to assess whether the product obtained in the low-temperature solid-state reaction was a remnant metastable phase or a stable phase. In the future, a deeper understanding of quantitative reactions will allow us to predict more detailed reaction processes with high accuracy. Also, to determine the parameters that govern the product selectivity, the experimenter must be aware of and record various things such as the state of the raw materials, the material of the crucible, the dew point, and the cooling rate.

## List of Publications

Original articles regarding this study are as follows

### Chapter 2

“Selective Metathesis Synthesis of  $\text{MgCr}_2\text{S}_4$  by Control of Thermodynamic Driving Forces”

A. Miura, H. Ito, C. J. Bartel, W. Sun, Nataly Carolina Rosero-Navarro, K. Tadanaga, H. Nakata, K. Maeda, and Gerbrand Ceder

*Materials Horizons*, 2020, **7**, 1310. DOI: 10.1039/c9mh01999e

### Chapter 3

“Kinetically Stabilized Cation Arrangement in  $\text{Li}_3\text{YCl}_6$  Superionic Conductor during Solid-State Reaction”

H. Ito, K. Shitara, Y. Wang, K. Fujii, M. Yashima, Y. Goto, C. Moriyoshi, Nataly Carolina Rosero-Navarro, A. Miura, and K. Tadanaga

*Advanced Science*, 2021, **8**, 2101413. DOI: 10.1002/advs.202101413